minerals

MDPI

Article

Unraveling the Protracted Magmatic Evolution in the Central Urumieh–Dokhtar Magmatic Arc (Northeast Saveh, Iran): Zircon U-Pb Dating, Lu-Hf Isotopes, and Geochemical Constraints

Mohammad Goudarzi [1,2,*], Hassan Zamanian [3], Urs Klötzli [2], Jiří Sláma [4], Jitka Míková [5], Jolanta Burda [6], David R. Lentz [7], Matee Ullah [2] and Jiranan Homnan [2]

1 Department of Geology, Faculty of Basic Sciences, Lorestan University, Khorramabad 6815144316, Iran
2 Department of Lithospheric Research, Faculty of Earth Sciences, Geography and Astronomy, University of Vienna, 1090 Vienna, Austria; urs.kloetzli@univie.ac.at (U.K.); mateeu89@univie.ac.at (M.U.); homnanj94@univie.ac.at (J.H.)
3 Department of Geology, Faculty of Sciences, University of Tehran, Tehran 1417935840, Iran; hasanzamanian@yahoo.com
4 Institute of Geology, Academy of Sciences of the Czech Republic, 165 00 Prague, Czech Republic; slama@gli.cas.cz
5 Czech Geological Survey, 118 00 Prague, Czech Republic; jitka.mikova@seznam.cz
6 Institute of Earth Sciences, Faculty of Natural Sciences, University of Silesia in Katowice, 41-200 Sosnowiec, Poland; jolanta.burda@us.edu.pl
7 Department of Earth Sciences, University of New Brunswick, Fredericton, NB E3B 5A3, Canada; dlentz@unb.ca
* Correspondence: goudarzi.mo@fs.lu.ac.ir

Abstract: Cenozoic plutonic rocks in northeast Saveh, part of the central Urumieh–Dokhtar Magmatic Arc (UDMA) in Iran, comprise monzonite, monzodiorite, gabbro, and gabbrodiorite. Geochemical, zircon U-Pb geochronology, and Hf isotopic data reveal that these plutonic rocks belong to a medium-K calc-alkaline, metaluminous series with arc-related signatures. Zircon U-Pb ages (ca. 60 to 3 Ma) indicate prolonged magmatic evolution from the Middle Paleocene to the Middle Pliocene. Contrary to earlier reports of a 15 Ma period of reduced magmatic activity (ca. 72–57 Ma), our data indicate a shorter interval (ca. 10–12 Ma) during which magmatic activity decreased significantly. Key magmatic pulses occurred during the Late Eocene (ca. 40–47 Ma), Early Miocene (ca. 23–18 Ma), and Late Miocene–Pliocene (ca. 11–5.2 Ma), with geochemical data indicating a subduction-related origin. The most recent magmatic pulses in the central UDMA, potentially extending across the entire UDMA, are dated between 5 and 2.5 Ma, identified in a cluster of zircons from gabbroic rocks, which could correspond to the concluding stages of slab steepening related to continental subduction. Zircon εHf(t) values (−11.43 to 12.5) and geochemical data suggest fractional crystallization, crustal assimilation, and mantle-derived melts. The clinopyroxene crystallization temperatures (1150–1200 °C) and supporting geochemical data imply that magma was produced in a metasomatized spinel–lherzolite mantle at depths <80 km. This generation is associated with asthenospheric upwelling and slab rollback, which, in turn, triggered the partial melting of the lithosphere and fueled the region's magmatic activity.

Keywords: Urumieh–Dokhtar magmatic arc; geochemistry; U-Pb geochronology; Lu-Hf isotopes; mineral chemistry; multi-stage magmatism

check for updates

Academic Editors: Ilya Bindeman and Federica Zaccarini

Received: 3 February 2025
Revised: 19 March 2025
Accepted: 31 March 2025
Published: 3 April 2025

Citation: Goudarzi, M.; Zamanian, H.; Klötzli, U.; Sláma, J.; Míková, J.; Burda, J.; Lentz, D.R.; Ullah, M.; Homnan, J. Unraveling the Protracted Magmatic Evolution in the Central Urumieh–Dokhtar Magmatic Arc (Northeast Saveh, Iran): Zircon U-Pb Dating, Lu-Hf Isotopes, and Geochemical Constraints. *Minerals* **2025**, *15*, 375. https://doi.org/10.3390/min15040375

Copyright: © 2025 by the authors. Licensee MDPI, Basel, Switzerland. This article is an open access article distributed under the terms and conditions of the Creative Commons Attribution (CC BY) license (https://creativecommons.org/licenses/by/4.0/).

1. Introduction

Calc-alkaline magmas form a key component in the evolution and formation of the continental crust, originating from diverse sources like the sub-arc metasomatized mantle, subducted sediments, and enriched lithospheric mantle that offer valuable insights into crustal recycling and tectonic processes. Unlike tholeiitic magmas, calc-alkaline magmas are distinguished by their higher water content, higher oxygen fugacity, elevated concentrations of large ion lithophile elements (LILEs), and depletion in high field strength elements (HFSEs). These petro-geochemical features reflect the influence of subduction-modified sources and mantle wedge metasomatism. The ascent of these magmas through the thick continental lithosphere, particularly in convergent zones, leads to additional geochemical diversity through processes such as magma mixing, fractional crystallization, and crustal assimilation, e.g., [1–5]. Advancements in understanding the partitioning behavior of trace elements, like LILEs and HFSEs, have refined models of subduction zone magmatism, emphasizing the role of slab-derived fluids and mantle wedge processes, e.g., [2–6]. Additionally, radiogenic isotopic methods, such as U-Pb and Lu-Hf mineral dating, provide insights into the timing and sources of magmas, enhancing our understanding of mantle and crustal contributions in these tectonic settings, e.g., [7–13].

Cenozoic active-margin magmatism related to the evolution of the Neo-Tethys has been identified in circus Neo-Tethyan regions, such as Iran, central and eastern Turkey, and the Caucasus. Research on the evolution of the Neo-Tethys in Iran is mainly focused on stratigraphy, paleontology, tectonic processes, and igneous activity related to the subduction and closure of Neo-Tethys, e.g., [14–22].

While extensive research has been conducted on crust–mantle interactions in Cenozoic continental arc environments, such as in the Andes [23], Indonesia [24], and Turkey [25], studies on the Cenozoic arc of Iran remain limited. The Urumieh–Dokhtar Magmatic Arc (UDMA) is a prominent volcanic arc system formed along the northern margin of the Neo-Tethys Ocean, and despite the active ongoing subduction, the magmatic activity in the UDMA was largely shaped by an Eocene flare-up during the Eocene–Oligocene for ~17 my from ca. 55 to ca. 37 Ma, which represents a significant period of intensified volcanic activity driven by crustal melting and mantle-derived magmas, e.g., [26–29]. This flare-up is a key feature of the broader Neo-Tethys realm, highlighting regional variations in magmatic processes linked to tectonic evolution. Studies report magmatic activity in the UDMA during the Late Eocene to Early Miocene, e.g., [28,30–35] and between 26 and 15 Ma, e.g., [30,32,36], as well as <10 Ma in the central UDMA [8,37].

The geochemical characteristics of UDMA igneous rocks indicate a continuous magma supply from subduction sources. However, the central UDMA, especially the Saveh area, remains thoroughly under-explored. Its magmatic history is not well understood, and the age and genetic connections of UDMA igneous rocks need further study.

This study, for the first time, identifies and examines several plutonic bodies in the northeast Saveh at the central UDMA (Figure 1). Some of these intrusive bodies are absent from the fundamental geological maps of the Saveh area (particularly the 1:100,000 scale map, Ref. [38], used in this study). Unlike the intrusive bodies in northwest Saveh, the northeastern intrusive rocks have neither been identified nor studied in detail. This underscores the necessity for comprehensive geochronological and geochemical analyses to enhance our understanding of the magmatic and tectonic evolution of the central Urumieh–Dokhtar Magmatic Arc (UDMA) and potentially the entire arc system. Furthermore, this study has the potential to identify the youngest intrusive rocks in the central segment of the UDMA, offering significant insights into the final stages of magmatic activity in the UDMA. The identification and characterization of previously undocumented plutonic bodies underscore the complexity of magmatic activity in the central UDMA.

These findings contribute to the broader understanding of subduction-related magmatism and crustal development in the region. By deciphering the multi-stage magmatic events in northeast Saveh, this study aims to enhance models of tectono-magmatic evolution and provide new perspectives on the processes governing continental crust formation in convergent margin systems. This study employs an integrated approach combining new data from zircon U–Pb geochronology, zircon Lu-Hf isotopic analysis, whole-rock geochemistry, and mineral chemistry to unravel the temporal and petrogenetic characteristics of magmatism in the northeast Saveh area. This research not only enhances our understanding of the magmatic processes within the UDMA but also provides broader insights into the tectonic evolution of the Neo-Tethyan orogenic belt. The findings of this study are anticipated to enrich the global database on magmatic and tectonic processes, offering a robust framework for future investigations in comparable geological settings.

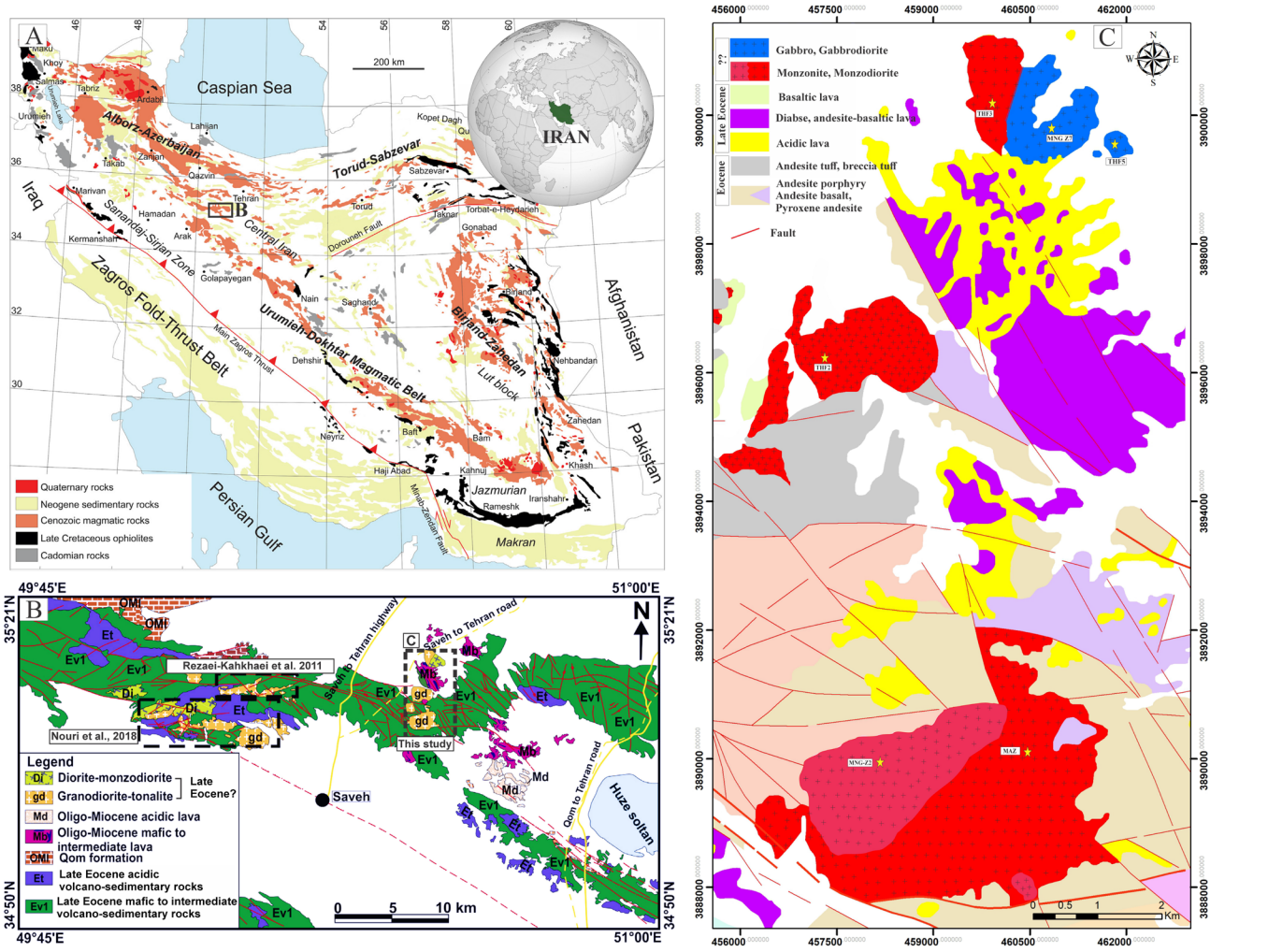


Figure 1. (**A**) Geology map of Iran [39]. (**B**) Geological map of the central UDMA, modified after [40] and location of Northwest Saveh magmatic rocks based on [40,41]. (**C**) Simplified geological map of northeast Saveh based on satellite data, fieldwork, and the geological map of Zaviyeh 1:100,000; Ref. [42] with approximate sample locations.

2. Geological Background

2.1. Regional Geology

The Alpine–Himalayan orogenic belt formed in the late Mesozoic–Cenozoic from Neo-Tethys subduction beneath continental plates, producing calc-alkaline to high-K magmatic rocks in Anatolia, the Caucasus, Iran, and the Lhasa terrane, e.g., [9,39,43,44] (Figure 1A).

Magmatic activity in Iran–eastern Turkey–the Caucasus began in the Late Cretaceous (105–95 Ma) and lasted about 80 My, e.g., [45–48], ending with the Afro-Arabian–Eurasian collision in the Miocene, e.g., [31,37,44,49–51]. The widespread Eocene–Middle Miocene magmatic rocks—including the Urumieh–Dokhtar Magmatic Arc and high-K igneous rocks in NW, NE, and SE Iran, as well as NE Turkey—further confirm Neo-Tethys subduction, e.g., [25,28,31,39,43,45,50–55].

The UDMA consists of crustal thick (~4 km) Cenozoic extrusive and intrusive rocks (Figure 1A) associated with volcanoclastic units from the Eocene to Quaternary, e.g., [28,31,56–58]. Ref. [59] suggests that the Eocene marked a significant tectonic regime change from an extensional to a compressional plate margin.

Many studies support the formation and emplacement of the UDMA during the late Eocene to early Miocene, e.g., [26,28,31,35,37,39,60,61].

The magmatism in the central UDMA occurred in two episodes: 42–38 Ma and 25–18 Ma [44]. The oblique rollback of the Neo-Tethys slab from 42 to 25 Ma contributed to the westward–youngling trend of magmatism in this zone, while older magmatism in the eastern parts predates this rollback phase, e.g., [9,40,41,44,62–65]. The youngest magmatism, reported to be less than 10 My, is documented in the central UDMA [8,37].

The central UDMA's plutonic rocks (Figure 1B) include gabbro, diorite, monzonite, quartz monzonite, and granodiorite to granite compositions with Oligo–Miocene ages. The Eocene volcanic rocks mainly comprise basalt, dacite, and andesite, erupted as pyroclastic and lava flows and ignimbrite rocks [65].

The initial magmatic activity in this volcanic complex involved the eruption of rocks with both calc-alkaline and alkaline geochemical signatures. Later stages witnessed the rise of intermediate to alkaline basaltic rocks enriched in elements like Sr, Rb, Ba, and K. This geochemical trend suggests that the region underwent an extension during this period [62]. Regional structural studies in the Saveh area reveal dominant trends oriented northwest, northeast, and east–west. The major faults within the region typically exhibit strike-slip and oblique-slip characteristics, with thrust faulting being less common. This pattern is consistent with a regime dominated by shear–compressive forces. Thrust faulting appears to represent a later phase in the evolution of these fault systems, as evident in certain faults like the Saveh Fault (Figure 1B).

As stated, geological observations indicate an extensional tectonic regime in the intra-arc setting during the Eocene, characterized by uplift, normal faulting, and magma eruption. In the late Eocene–Oligocene, this regime transitioned to a compressional phase, leading to the development of a dextral shear zone and activation of strike-slip faults, reflecting regional stress variations [31,40]. These compressive forces altered the structural behavior from ductile to brittle, resulting in a prominent east–west structural trend in the central area. In the early stages, magmatic intrusions were emplaced within a transtensional setting at deep crustal levels, indicating post-collisional extensional features cf. [66].

2.2. Geological Overview and Petrographic Observations of the Study Area

The studied area is located in northeast Saveh in the central part of the UDMA and ca. 100 km southwest of Tehran (Figure 1C). The intrusive rocks are exposed in a ca. 15 × 7 km area northeast of Saveh (Figure 1). Magmatic activities in this region have been influenced by significant west–northwest to east–southeast–trending faults, such as Rangezard, Takht-e-Chaman, and Abbas Abad (Figure 1B,C), which have acted as magma pathways and controlled the alignment of volcanic centers. Additionally, several smaller northwest–southeast–trending faults have influenced magma ascent and later displaced igneous bodies, all of which are associated with the Alpine orogeny [42].

Geological mapping and detailed fieldwork of the area reveal two main igneous rock types, including monzonite–monzodiorite and gabbro–gabbrodiorite. They were intruded into alternating sequences of volcanic rocks of an acidic to basic composition. Although the contact between volcanic and intrusive rocks is usually gradational, the intrusive types are distinct and easily recognized in outcrops.

The outcrops of the monzonite–monzodiorite unit comprise part of the northeast Saveh area's main elevations (Figure 2A,B). Microscopic studies reveal that this unit yield exhibits granoblastic and porphyritic textures. Major minerals include plagioclase, potassium feldspar, clinopyroxene, hornblende, and quartz, while accessory minerals consist of apatite, zircon, and opaque minerals (iron oxides). Secondary minerals, including chlorite, clay minerals, carbonate, and epidote, are also present. Abundant euhedral to subhedral tabular plagioclase is the most common constituent of the rock, showing signs of corrosion in some cases and infilled with secondary minerals such as chlorite (Figure 3A). Plagioclase phenocrysts are occasionally carbonatized and frequently exhibit extensive sericitization, with intense alteration in some instances, leaving only minor remnants of the crystals and dominating a large volume of the groundmass microcrystals (Figure 3B,C). Subhedral to anhedral clinopyroxene crystals constitute up to 20–25% of the sample in some cases (Figure 3A). Amphibole occurs in a wide range of grain sizes from fine-grained microcrystals to larger crystals that stand out within the groundmass, with moderate to low chloritization. Tourmaline crystals are occasionally observed in abundance in some samples, suggesting the incorporation of a boron-bearing high-temperature fluid in some places (Figure 3D).

The main outcrop of the gabbro–gabbrodiorite unit is located in the northeastern part of the study area, exhibiting a comparable dark-gray field appearance and partially consolidated morphology. Its composition includes gabbro, gabbrodiorite, and diorite gabbro (Figure 2C–E). Petrographic studies of the samples reveal granoblastic, heterogranular, hypidiomorphic, anti-rapakivi, and/or granular textures. Plagioclase and pyroxene crystals, varying in size, are the main constituents of the rock (Figure 3E,F). These are often subhedral to euhedral, with large crystals sometimes constituting 60–65% of the rock. Some crystals exhibit twinning and are moderate to highly uralitized, and in some cases, pyroxene is replaced by amphibole. Hornblende microcrystals show low to moderate alteration and chloritization and, in some cases, have led to the formation of actinolite in the samples (Figure 3G). Plagioclase, ranging from phenocrysts to microcrysts and microlites, exhibits moderate to high alteration and argillization and sericitization and sometimes shows an anti-rapakivi texture (Figure 3G). The intensity of alteration is high in some crystals, leaving only a small portion of the primary mineral. The margins of some crystals were reactive and in disequilibrium, showing epidote or chlorite replacing the space created by corrosion (Figure 3F,I). Euhedral to subhedral pyroxene crystals with octagonal cross-sections, ranging from micro-phenocrysts to microcrystals, exhibit moderate to severe alteration and chloritization (Figure 3A). Radiating amphibole crystals are observed in abundance in some samples (Figure 3H). Minor accessory minerals include zircon and apatite, while secondary and alteration minerals include epidote, clay minerals, carbonate, iron oxide and hydroxide, and chlorite.

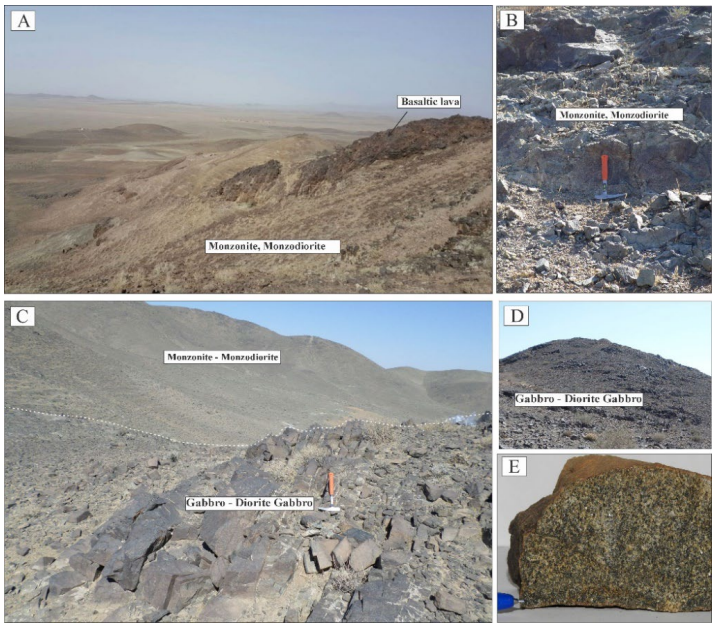


Figure 2. (**A**) General view of monzonite–monzodiorite rock. (**B**) close up view of monzonite, Monzodiorite. (**C**,**D**) General view of the plutonic outcrops. (**E**) close up view of gabbroic rock.

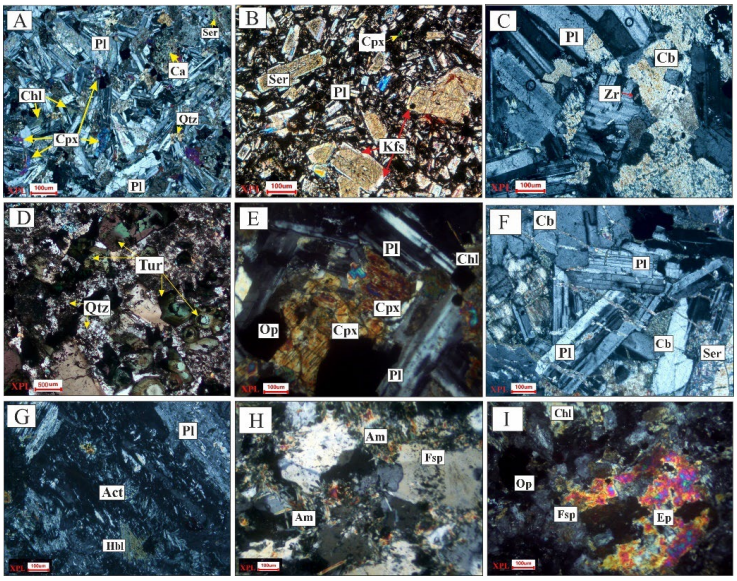


Figure 3. Photomicrographs (crossed polarized light) of (**A**) coarse plagioclase crystals with small clinopyroxene crystals inclusions, where some minerals have been replaced by carbonate and chlorite; (**B**) fine-grained groundmass containing plagioclase microlites and microcrystals and sericitized plagioclase replaced by K-feldspar in the rim with hypo-crystalline texture; (**C**) aphitic texture and carbonate alteration with zircon inclusions in monzodiorite; (**D**) tourmalinization in quartz monzonite under the influence of boron-containing fluids; (**E**) coarse crystal of clinopyroxene and plagioclase with polysynthetic twinning and chloritized Fe-Mg minerals; (**F**) sericitization of plagioclase crystals along polysynthetic twining and fracture filling with carbonate in gabbrodiorite; (**G**) altered hornblende microcrystals that caused the creation of fine and needly actinolites and plagioclase with anti-rapakivi texture; (**H**) radial and tabular amphibole microcrystals with microcrystalline quartz; (**I**) argillized alkali feldspar microcrystals and plagioclase crystals with epidote alteration. Mineral abbreviations [67]: Pl: plagioclase, Ep: epidote, Am: amphibole, Cb: carbonate, Ser: sericite, Cpx: clinopyroxene, Fsp: feldspar, Chl: chlorite, Op: opaque minerals, Act: actinolite, Qtz: quartz, Zr: zircon, Tur: tourmaline.

3. Analytical Methods

The analytical methods are detailed in Supplementary File S1, which also specifies the instrumental parameters, experimental conditions, reference materials, and data reduction procedures. Fifty samples were selected for lithologic and petrographic investigation, and thin sections were prepared for detailed analysis. Of these, 21 minimally altered samples (11 from monzonite–monzodiorite pluton and 10 from gabbro–gabbrodiorite rocks) were chosen for major and trace element analysis. Major-element concentrations were determined in clinopyroxene (19 spots), orthopyroxene (20 spots), and plagioclase (72 spots for monzonitic rocks and 42 spots for gabbroic rocks). Additionally, six samples were selected for zircon U-Pb dating and Lu-Hf isotope systematics—four from the monzonitic–monzodioritic rocks (THF2, THF3, MNG-Z2, and MAZ) and two from the gabbroic–gabbrodioritic rocks (THF5 and MNZ-Z7).

4. Results

4.1. Whole-Rock Geochemistry

We provide the major element data for whole-rock samples collected from the northeast Saveh plutonic rocks in Supplementary Table S1. The SiO_2 value varies from 51.1 to 60.1 wt.%, and Al_2O_3 ranges from 14.2 to 17.7 wt.%. The total amount of alkali elements varies from 3.1 to 8.79 wt.%. In the total alkali silica diagram [68], the northeast Saveh magmatic samples plot mainly in the fields for monzonite, monzodiorite, gabbro, and gabbrodiorite (Figure 4A). The $Al_2O_3/(CaO + Na_2O + K_2O)$ (A/CNK) molecular ratio varies between 0.6 and 1, indicating metaluminous compositions.

The presence of specific characteristics, such as $Na_2O > K_2O$ and A/CNK < 1, is a hallmark of I-type rocks [69].

In the SiO_2 vs. $FeO^t/(FeOt + MgO)$ diagram (Figure 4B), the northeast Saveh samples, except one of the gabbroic samples, show a low FeOt/(FeOt + MgO) (0.47–0.65) and are thus classified as magnesian granitoids [70]. In the Nb + Y versus Rb plot [71], the samples are classified as I-type granitoids (Figure 4C). Through prolonged fractionation of silicic magmas, Cu, Au, Pb, Zn, and Fe become depleted, and further dilution occurs due to increasing continental crustal contamination. While residing in the crust of subduction zones, these magmas often mix with new mantle-derived magma. This interaction disrupts their evolution via fractional crystallization, maintaining high levels of compatible elements like copper, which is beneficial for forming magmatic hydrothermal mineral deposits in the study area (e.g., Rangraz and Mamuniyeh deposits) [65,72–77]. Based on the Yb vs. La/Yb plot [78] that distinguishes normal magmatic arc rocks from adakites (Figure 4D), the northeast Saveh magmatic rocks do not show adakitic affinity, such as high La/Yb and Sr/Y ratios, and they display calc-alkaline characteristics and normal volcanic arc rock features, such as low Sr and high Y and Yb values. It is also noteworthy that the northeast Saveh samples are metaluminous [65]. Nonetheless, the mineralogical composition of the northeast Saveh samples, which includes hornblende, biotite, magnetite, zircon, and apatite and the absence of Al-rich minerals like corundum, cordierite, and topaz, along with the lack of crustal enclaves, indicate their metaluminous nature. The differentiation of hornblende or water content in the melting zone [79] may also account for this phenomenon.

Additionally, the high average values of Na_2O/K_2O (8.6) and the combined $Na_2O + K_2O$ (5.33 wt%) exhibit the sodic nature of the rocks. The K_2O content shows a range between 0.30 and 0.81 wt% and has calc-alkaline affinities in the K_2O vs. SiO_2 [80] and Zr vs. Y [81] diagrams (Figure 5A,B). The high K_2O content in some samples may be due to the sericitization of plagioclase and pyroxene crystals.

In the Harker diagrams (Figure 6), Al_2O_3, MgO, Fe_2O_3, CaO, K_2O, and, to some extent, TiO_2 show a descending trend with increasing SiO_2, while Na_2O_3, P_2O_5, and K_2O show an ascending linear trend. The observed negative correlations between Fe_2O_3, MgO, Al_2O_3, and, to some extent, TiO_2 with SiO_2 can be explained by the crystallization of clinopyroxene, olivine, hornblende, magnetite, and ilmenite. Additionally, the reduction in Al_2O_3 and CaO is likely due to the fractionation of Ca-rich plagioclase. Moreover, the increase in K_2O with magma evolution suggests that K-feldspar is not the primary fractionating phase in these magmas.

The chondrite-normalized REE patterns of the northeast Saveh intrusive rocks [82] exhibit an enrichment of LREEs compared to HREEs, with $(La/Yb)_n$ values ranging from 4.5 to 12.1. These patterns lack pronounced negative Eu anomalies (Figure 7A), as indicated by Eu/Eu* ratios ranging from 0.95 to 1.65.

The negative slope in the primitive mantle-normalized spider diagrams [82] indicates a relative enrichment of LILEs compared to HFSEs. This depletion of HREEs is typical of subduction environments and calc-alkaline magmas from volcanic arcs at continental active margins, e.g., [71,83]. The strong positive Pb anomalies are likely due to the crustal contamination of the magma that formed these rocks (Figure 7B).

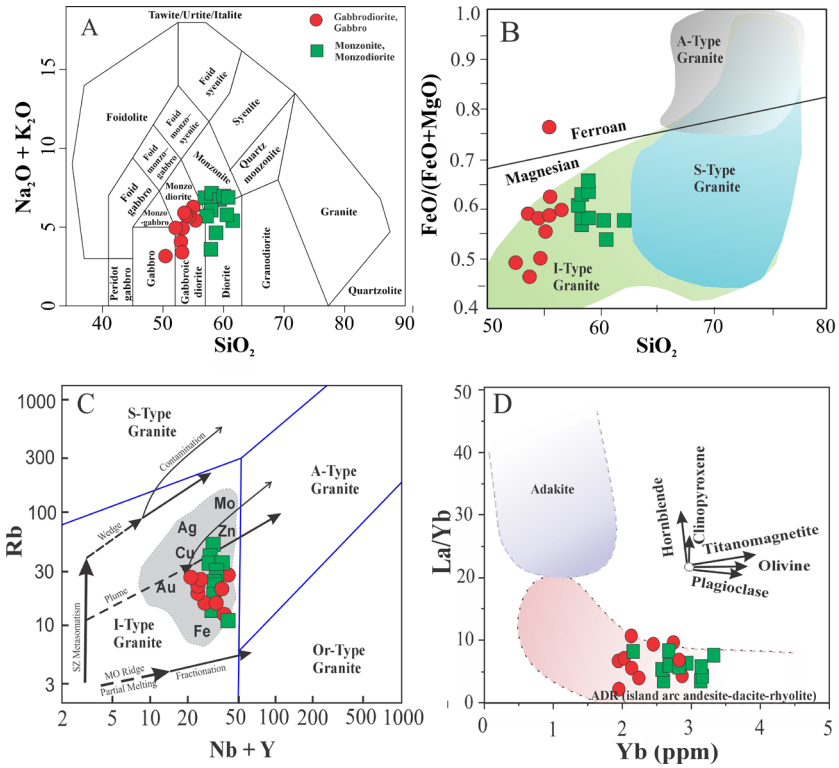


Figure 4. Classification of northeast Saveh plutonic rocks. (**A**) SiO_2 (wt.%) versus $Na_2O + K_2O$ (wt.%) binary diagram [68]. (**B**) SiO_2 (wt.%) versus FeOt/(FeOt + MgO) diagram (after Frost et al., 2001 [70]). (**C**) Rb (ppm) versus Nb + Y (ppm) diagram displays the trace element compositions of granites associated with different mineralization types, showing the impact of various processes and source compositions on trace element patterns (modified after [84]. (**D**) La/Yb versus Yb plot [78] is presented to further illustrate these trends.

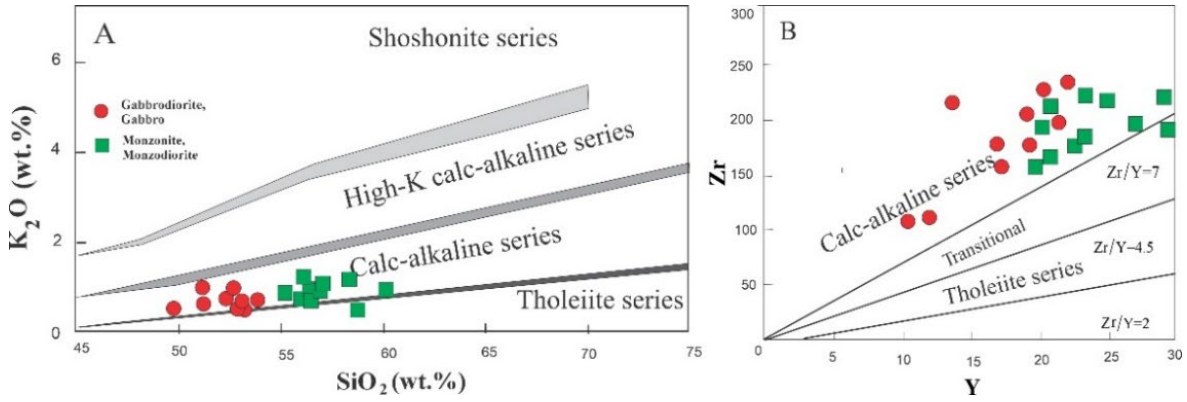


Figure 5. (**A**) K_2O (wt.%) vs. SiO_2 (wt.%) diagram showing the calc-alkaline nature of the northeast Saveh rocks [80]. (**B**) Zr versus Y [81].

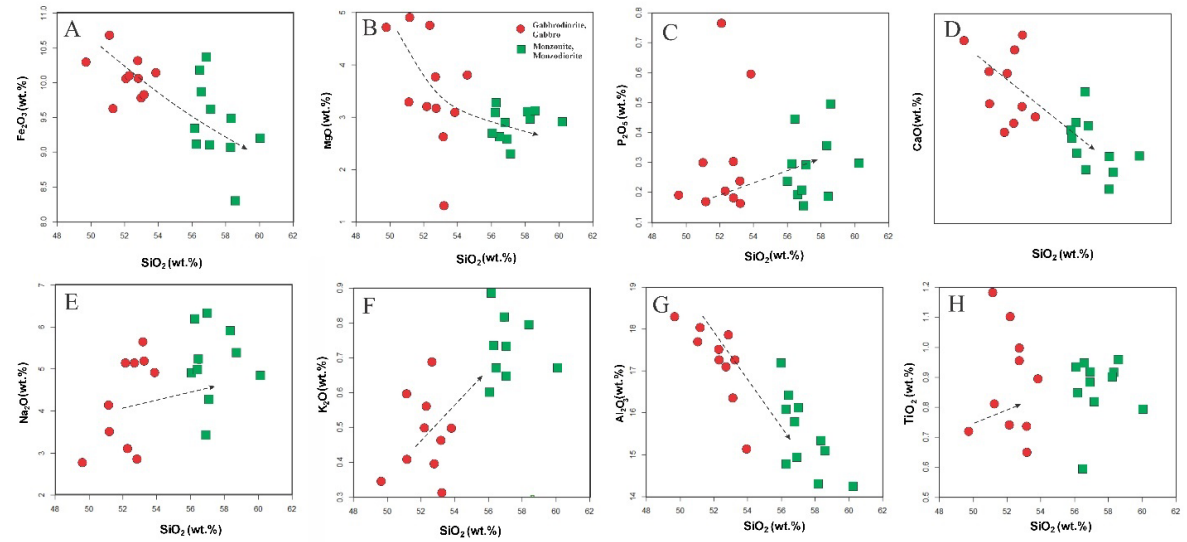


Figure 6. Major oxides vs. SiO_2 (wt.%) content for northeast Saveh intrusive rocks. (**A**) SiO_2 (wt.%) vs. Fe_2O_3 (wt.%). (**B**) SiO_2 (wt.%) vs. MgO (wt.%). (**C**) SiO_2 (wt.%) vs. P_2O_5 (wt.%). (**D**) SiO_2 (wt.%) vs. CaO (wt.%). (**E**) SiO_2 (wt.%) vs. Na_2O (wt.%). (**F**) SiO_2 (wt.%) vs. K_2O (wt.%). (**G**) SiO_2 (wt.%) vs. Al_2O_3 (wt.%). (**H**) SiO_2 (wt.%) vs. TiO_2 (wt.%).

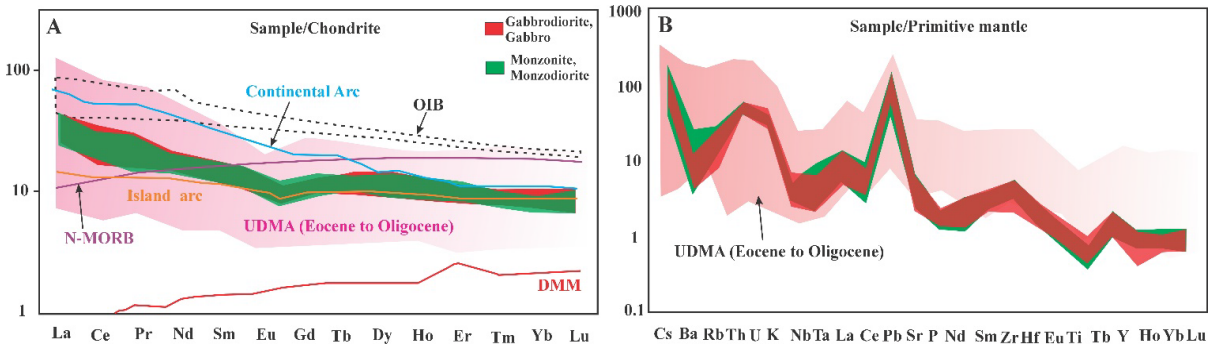


Figure 7. (**A**) Chondrite-normalized REE spider diagram showing patterns for the northeast Saveh plutonic rocks (chondrite values from [85]. (**B**) Primitive mantle-normalized trace-element spider diagram for the northeast Saveh samples, normalizing values [82]. DMM (depleted MORB mantle) and OIB (ocean island basalt).

4.2. Mineral Chemistry

The results of the chemical analysis of plagioclases, orthopyroxene, and clinopyroxenes in monzonitic and gabbroic rocks from the northeast Saveh are listed in Supplementary Tables S2 and S3. Plagioclase and pyroxene are key and important minerals in determining the magmatic origin, tectonic setting, and physio-chemical conditions, including temperature, pressure, and partial oxygen pressure. Plagioclase is one of the main minerals forming the intermediate rocks in northeast Saveh. To accurately determine the chemical composition of monzonitic plagioclases, 72 points were chemically analyzed, and for gabbroic units, 42 points were analyzed. The analysis was conducted exclusively on the unaltered portions of plagioclase. The results of the chemical analysis of plagioclases in the Or-Ab-An ternary plot [86] show compositions ranging from andesine to bytownite (An 44–83) for monzonitic rocks and andesine to labradorite (An 40–69) for gabbroic rocks (Figure 8A). The CaO content in plagioclase from monzonitic and gabbroic rocks varies from 9.2 to 17.2 wt.% and 8.3 to 14.3 wt.%, respectively. The Na_2O content in plagioclase from monzonitic and gabbroic rocks varies from 9.2 to 17.2 wt.% and 8.3 to 14.3 wt.%, respectively. The Al_2O_3 content in plagioclase from monzonitic and gabbroic rocks ranges from 26.5 to 33.1 wt.% and 25.6 to 31 wt.%, respectively. Additionally, the K_2O content in plagioclase from monzonitic and gabbroic rocks varies from 0.06 to 0.62 wt.% and 0.2 to 0.79 wt.%, respectively.

To accurately determine the chemical composition of pyroxenes, 19 points from clinopyroxene and 19 points from orthopyroxene were chemically analyzed (Table S3). The composition of pyroxenes in the monzonitic rocks of northeast Saveh is of the augite type, while in the gabbroic rocks, it includes both augite and enstatite (Figure 8B). The average MgO content in clinopyroxene (14.2 wt.%) is higher than the average FeO content (11.8 wt.%). Conversely, in orthopyroxene, the average FeO content (25.7 wt.%) is higher than the average MgO content (18.7 wt.%).

The studied pyroxenes are plotted in the Q-J diagram [87] within the field of sodium-free and calcium–magnesium–iron pyroxenes (Figure 8C). The J and Q in this diagram indices include $Ca^{2+} + Mg^{2+} + Fe^{2+}$ and J = 2Na, respectively.

The studied clinopyroxenes have compositions of Wo 35.2–44.9, En 36.5–44.4, and Fs 16.5–20.6. The orthopyroxenes have compositions of Wo 2.2–5.8, En 50.6–59.2, and Fs 38.4–46.6 (Table S3).

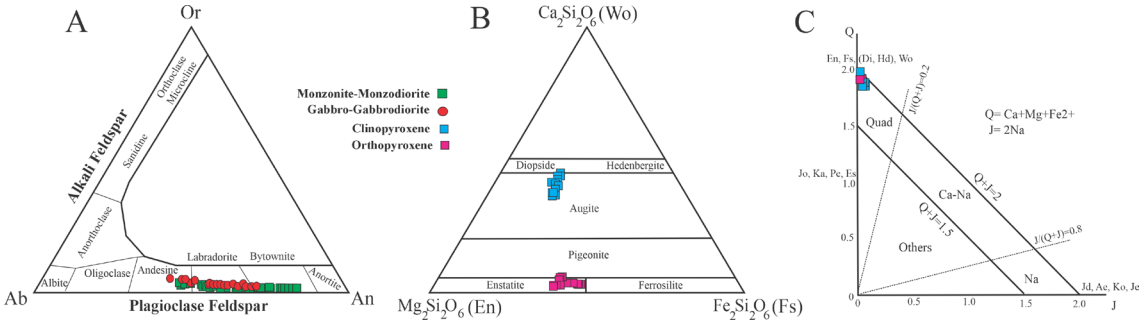


Figure 8. Mineral composition of plutonic rocks from northeast Saveh. (**A**) Plagioclases are compositions ranging from andesine to bytownite [86]. (**B**) $CaSiO_3$–$MgSiO_3$–$FeSiO_3$ diagram [87]. (**C**) All the pyroxenes of the northeast Saveh are in the range of (Mg-Fe-Ca) Quad (pyroxenes) J = 2Na, Q = $(Ca + Mg + Fe^{2+})$.

4.3. Zircon U-Pb Dating and Lu-Hf Isotopes

4.3.1. Zircon U-Pb Dating

Six samples from the intrusive rocks of northeast Saveh were dated by U-Pb geochronology. These samples comprised four monzonitic rocks (THF2, THF3, MAZ,

and MNG-Z2) and two gabbroic rocks (THF7 and MNG-Z7), as detailed in Supplementary Table S4 and illustrated in Figure 9. Zircons of various origins exhibit different morphologies and Th/U ratios.

Most of the zircons analyzed in this study exhibit euhedral shapes with elongated and wide prismatic pyramidal forms and display oscillatory zoning, which is indicative of magmatic origin. The zircon U-Pb results and representative CL images are illustrated in Figure 9, and the analytical dataset is given in Supplementary Table S4.

Typically, magmatic zircons have Th/U > 0.3, while metamorphic zircons generally exhibit Th/U ratios below 0.1 [88–90]. Nevertheless, through geological processes like anatexis, some altered magmatic zircons with Th/U ratios < 0.1 may form. In such cases, the low-Th/U rims represent the age of partial melting [91,92]. Zircons from the monzonite and gabbro are euhedral to subhedral, with length/width ratios of 1:1–5:1 (Figure 9), and exhibit concentric zonation without inherited cores and present well-developed oscillatory zoning (Figure 9). They also lack characteristics of crystallization or hydrothermal alteration, such as spongy texture and metamorphic effects [93,94].

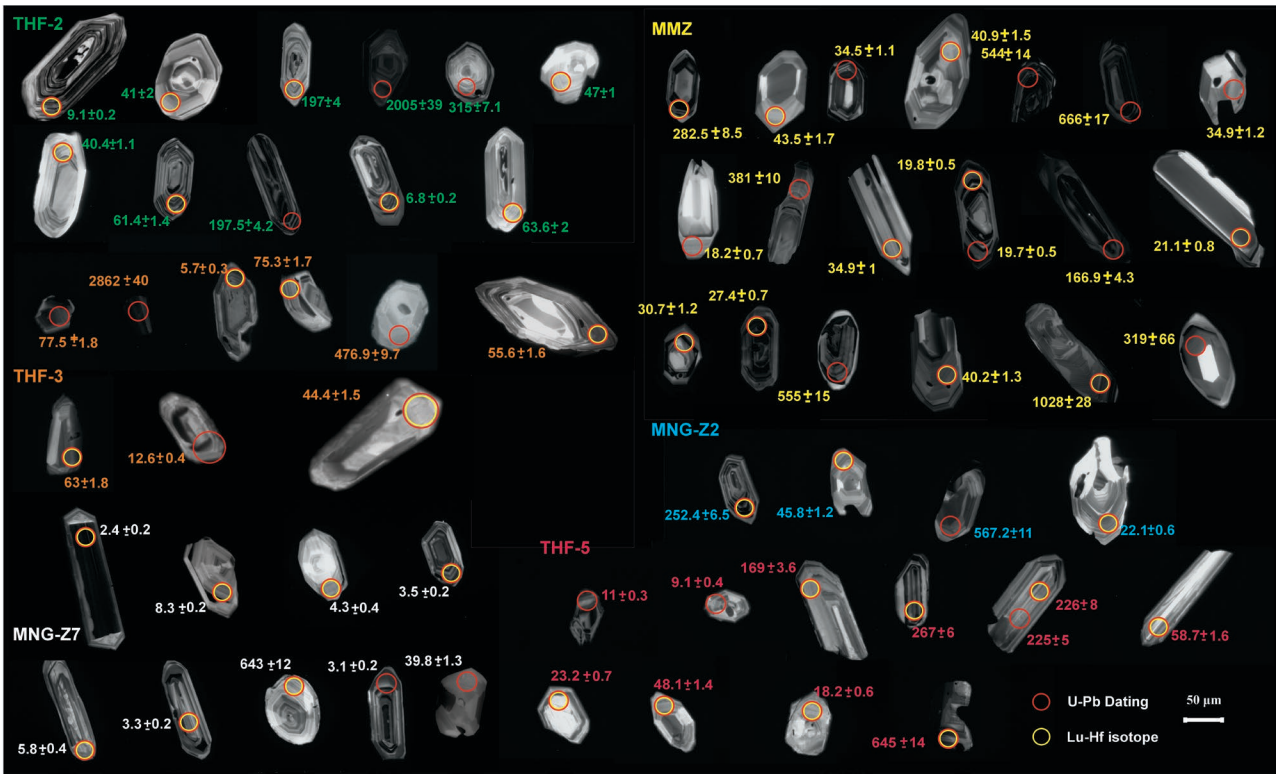


Figure 9. Cathodoluminescence (CL) images from zircons of plutonic rocks from northeast Saveh with U-Pb ages (Uncertainty: 2S). Red circles show the locations of U-Pb analysis spots, and yellow circles denote Hf isotope analyses.

Zircons from the monzonitic samples (THF2, THF3, MAZ, and MNG-Z2) are predominantly long prismatic in shape and vary in size from 50 to 200 μm and have patchy zonings. In cathodoluminescence (CL) imaging, these zircons predominantly exhibit magmatic concentric and oscillatory zoning, while a few grains display less distinct zoning patterns, suggesting different levels of solid-state recrystallization [95]. The rims cut across some inherited cores.

Three analyses yielded Mesoarchean (~2.8 Ga), Paleoproterozoic (~2 Ga), and Mesoproterozoic (~1 Ga) dates. Five analyses yielded Neoproterozoic dates (~544 Ma to 713 Ma). Six analyses yielded Paleozoic dates (~252 Ma to 476 Ma), and five grains yielded Mesozoic dates (~75 Ma to 197 Ma; Supplementary Table S4 and Figure 10A). Tertiary U-Pb zircon

ages found in the monzonitic sample are in the range of ca. 63.6 to 5.7 Ma (Figure 10B). Four main populations are characterized by weighted mean $^{206}Pb/^{238}U$ dates of 60.4 ± 0.83 Ma (n = 4, MSWD = 3) (Figure 10C), 42.7 ± 0.5 Ma (n = 7, MSWD = 2.1) (Figure 10D), and 20.8. ± 0.2 Ma (n = 5, MSWD = 1.5) (Figure 10E); the second and third dates (42.7 Ma and 20.8 Ma) are interpreted as the main crystallization age of the monzonitic rocks. Four other analyses also yielded a weighted mean $^{206}Pb/^{238}U$ age varying from 5.7 to 12.6 Ma (Supplementary Table S4).

Zircons from the gabbroic rocks (THF7, MNG-Z7) are prismatic to long prismatic in shape and vary in size from 50 to 200 µm. Two analyses yielded Neoproterozoic dates (~ 643–645 Ma). Four grains yielded late Triassic dates (~169 Ma to 266 Ma; Supplementary Table S4 and Figure 11A,B), and Cenozoic U-Pb zircon ages are in the range of ca., 58.76 to 2.4 Ma. The main populations of $^{206}Pb/^{238}U$ ages yielded a set of dates between 2.42 and 5.78 Ma, with a weighted mean $^{206}Pb/^{238}U$ date of 3.18 ± 0.07 Ma (n = 6, MSWD = 2.2) (Figure 11C). Moreover, there were three grains that yielded a set of dates between 8.28 and 11.03 Ma, with a weighted mean $^{206}Pb/^{238}U$ date of 9.7 ± 0.18 Ma (n = 3, MSWD = 4.1) (Figure 11C).

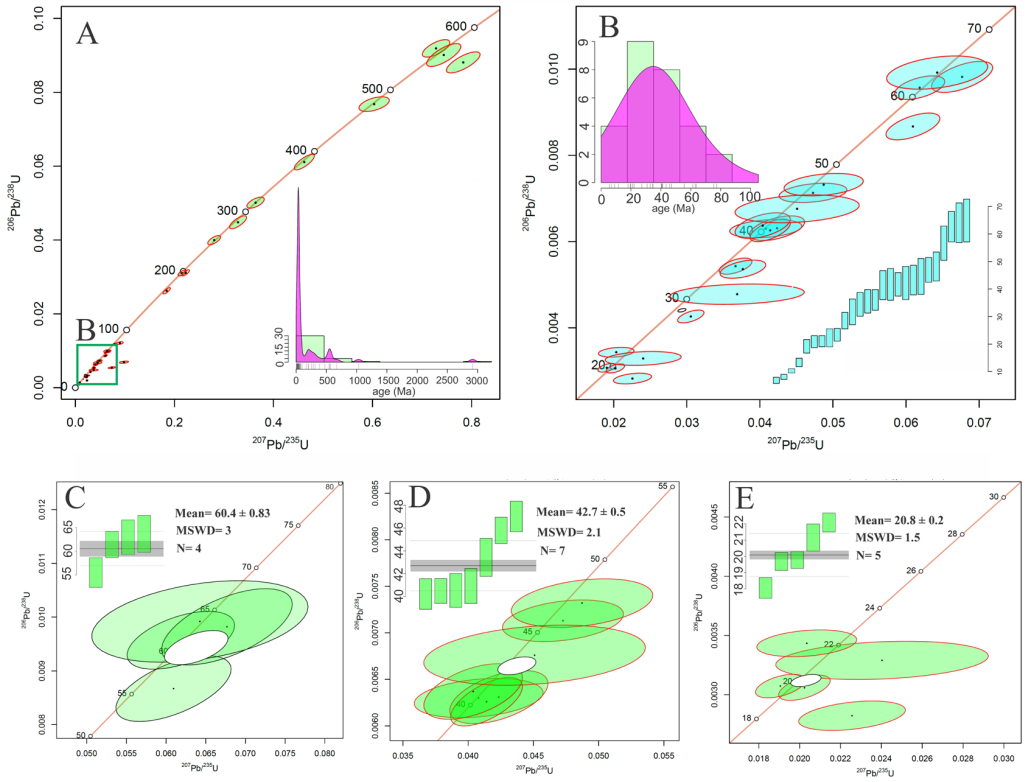


Figure 10. Zircon weighted mean $^{206}Pb/^{238}U$ ages and Wetherill Concordia diagrams of the monzonitic rocks of northeast Saveh. (**A**) Wetherill Concordia diagram plotting $^{206}Pb/^{238}U$ against $^{207}Pb/^{235}U$ for all zircon data, with 2σ analytical uncertainty ellipses. The reference concordia curves are also shown for comparison. (**B**) Histogram of the weighted mean ages along with a scatter plot illustrating the age distribution of the zircons, highlighting the variability among the samples with age < 70 Ma. (**C**) Scatter plot for a selected cluster of zircons with a weighted mean age of 60.4 ± 0.83 Ma and an MSWD of 3. (**D**) Similar scatter plot for a second cluster of zircons with a weighted mean age of 42.7 ± 0.5 Ma and an MSWD of 2.1, indicating distinct age characteristics compared to group. (**E**) Scatter plot for a third cluster of zircons with a weighted mean age of 20.8 ± 0.2 Ma.

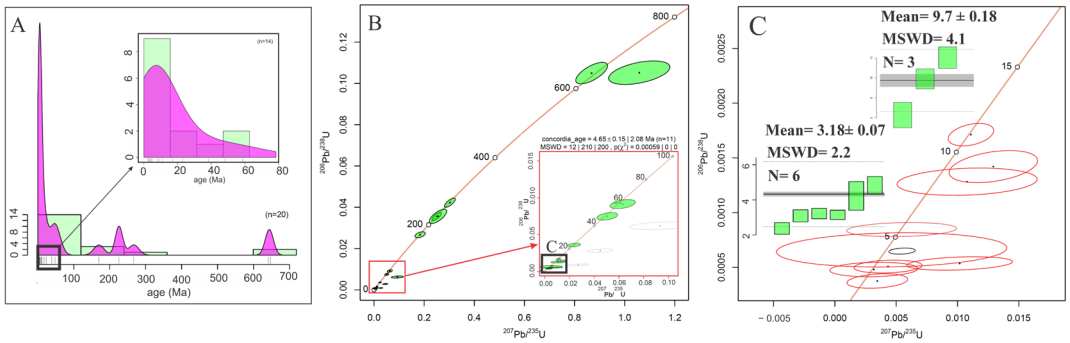


Figure 11. Zircon weighted mean $^{206}Pb/^{238}U$ ages and Wetherill Concordia diagrams of the gabbroic rocks of northeast Saveh. (**A**) Density plot (pink curve) and histogram (gray bars) of the measured zircon $^{206}Pb/^{238}U$ ages, showing the distribution of the main age populations. The inset provides a closer look at the age range of approximately 0–80 Ma, highlighting additional peaks. (**B**) Wetherill Concordia diagram ($^{206}Pb/^{238}U$ vs. $^{207}Pb/^{235}U$) for the same zircon dataset, with 2σ error ellipses. The reference concordia line is plotted in orange, and the inset zooms in on the younger zircon ages. Labels (<100 Ma) indicate approximate concordia ages. (**C**) Weighted mean ages for two distinct groups of zircon grains, indicated by their 2σ error ellipses (red). The first group yields a mean age of 9.7 ± 0.18 Ma, whereas the second group shows a mean age of 3.18 ± 0.07 Ma.

4.3.2. Zircon Lu-Hf Isotopes

Lu-Hf isotopic analysis was performed in the same CL domains as the U–Pb age measurements in 43 zircon grains from the gabbroic and monzonitic intrusions. Analysis was conducted on the Lu-Hf isotopic results for these rocks, which are presented in Figure 9 and listed in Supplementary Table S5. Most $^{176}Lu/^{177}Hf$ ratios are <0.002 (0.002411–0.0003998), except for two grains in the gabbroic intrusion (0.00388 and 0.003073), suggesting limited corresponding U-Pb ages, and an accumulation of radiogenic Hf was used for εHf(t) calculations (Figures 12 and 13). The εHf(i) CHUR values for zircons in the monzonites range from −5.5 to 12.5 (mean: 1.89), with their T_{DM} ages varying from 190.8 to 933.2 Ma (avg. 686.8 Ma). For the zircons in the gabbroic rocks, εHf(i) CHUR values range from −7.4 to 11.9 (avg. 2.56), and their T_{DM} ages range from 231.2 to 1132.5 Ma (avg. 703 Ma) (Supplementary Table S5). Negative εHf(i) values indicate that the sample is depleted in radiogenic ^{176}Hf compared to the chondritic uniform reservoir (CHUR). This suggests that the source of the sample likely had a lower Lu/Hf ratio compared to chondrites [96]. The $^{176}Hf/^{177}Hf$ ratios in Eocene zircons, with TDM ages spanning 0.23 to 0.9 Ga, indicate the involvement of Neo-Proterozoic and Meso-Proterozoic continental crust in shaping the Ediacaran–Cambrian basement of Iran [97]. Also, Miocene-Pliocene zircons show T_{DM} ages of ∼190 to 839 Ma, mirroring the extension of a Cenozoic continental arc on the Ediacaran–Cambrian crust (Figure 13). The variability in Hf isotopic values for Eocene zircons (−5.5 to +12.5) is likely associated with Hf heterogeneity. Generally, based on [98], several mechanisms are attributed to hafnium heterogeneity, including the assimilation of crustal components, and mixing of zircon-saturated mantle melts with different isotopic end-members, as well as the homogenization of melts that occurs after zircon dissolution.

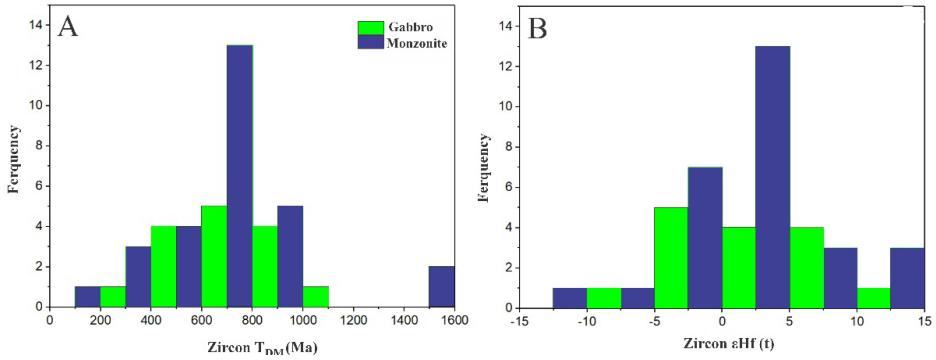


Figure 12. (**A**) Frequency histogram of εHf in northeast Saveh zircons. (**B**) Frequency histogram of TDM age in northeast Saveh zircons.

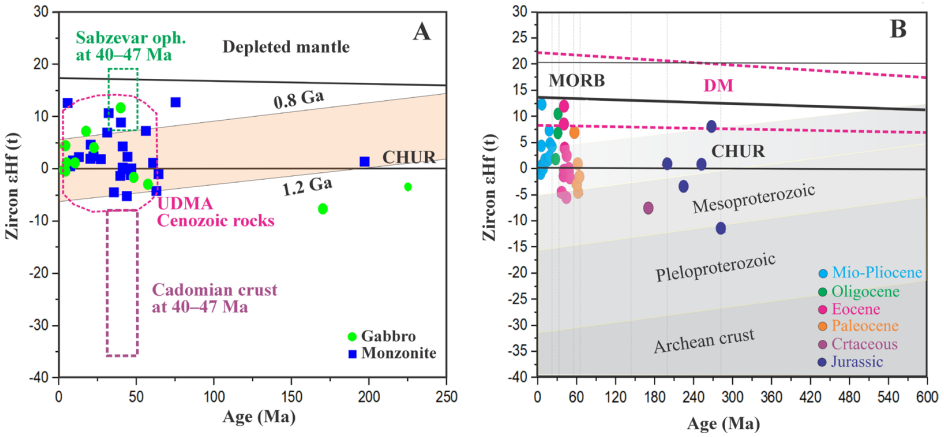


Figure 13. Variation diagram of εHf versus zircon age (Ma) for plutonic rocks from northeast Saveh. (**A**) Based on host rock, and (**B**) based on period. UDMA data according to [99], Cadomian rocks data according to [33], and Sabzevar ophiolites data according to [100].

5. Discussion

5.1. Tectonic Significance

The northeast Saveh samples display strongly fractionated REE patterns, characterized by enrichment in LILEs and depletion in HFSEs, which is consistent with an arc-like tectonic setting (Figures 6 and 7). Their classification within the field of active continental margin magmas, supported by Th/Yb versus Nb/Yb and Th/Yb versus Ta/Yb diagrams (Figure 14A,B), further corroborates their active continental margin origin. The rocks are positioned within the volcanic arc granite field on the Y versus Nb diagram according to [71] (Figure 14C). Consistent with these observations, the chemical data for the northeast Saveh samples, plotted on the Y vs. Zr discrimination diagram [101] (Figure 14D), clearly show that magmatic rocks in the area fall within the active continental margin and arc-related fields. This affiliation is in accordance with the findings from previous studies of the UDMA, e.g., [8,9,31,34,35,39,40,102–104].

The northeast Saveh samples exhibit high levels of SiO_2, ranging from 49.6 to 60.1 wt%, alongside extremely low concentrations of Cr (9–58 ppm) and Ni (3–13 ppm). These concentrations are considerably lower than the Cr and Ni (>1000 ppm and >400 ppm, respectively) typically associated with mantle-derived primary melts, as proposed by [83]. Furthermore, certain trace element ratios, like Y/Nb, Nb/La, Zr/Nb, and Nb/Ta, stand unaffected by fractionation. This stability makes them valuable for pinpointing sources of magma and evaluating the impact of the continental crust on magmatic rocks [105–108].

The Y/Nb ratio in granitoids derived from mantle melts is typically less than 1.2, whereas in crustal melts, it exceeds 1.2. The northeast Saveh samples exhibit Y/Nb ratios

ranging from 1.2 to 2.7, with an average of 1.88 ± 0.39 (standard deviation). These values indicate a predominant crustal contribution, though the lower end of the range suggests a minor mantle-derived component in the source magma [105].

According to [109], mantle-derived magmas typically have an average Nb/Ta ratio of 17.5, while crustal-derived magmas show ratios between 11 and 12. The Nb/Ta ratios for the Saveh samples range from 9.65 to 18.4, with a mean value of 14.5 ± 2.9, indicating a mixed contribution from both mantle and crustal sources.

Furthermore, according to [108], the average Nb/La and Zr/Nb ratios for primitive mantle are 1.0 and 6.3–7.6, respectively, while these ratios are 0.46 and 22–25 for continental rocks [108]. The Zr/Nb ratios for the northeast Saveh samples range from 10.3 to 26.9, with a mean of 16.5 ± 3.9, and the Nb/La ratios range from 0.3 to 1.2, with a mean of 0.6 ± 0.2. These values are more consistent with a crustal origin rather than a purely mantle-derived source. The ratios of incompatible trace elements indicate that the magmatic rocks from northeast Saveh were primarily derived from continental crust melts, with a possible minor contribution from mantle-derived material.

The analyzed samples exhibit Th/U ratios ranging from 3.6 to 7.3, with an average value of 5.3 ± 0.8. Based on [105], these samples predominantly plot within the transition zone between the N-MORB and continental crust fields (Figure 15).

Previous research indicates that the crustal component has a limited impact on the formation of NW Saveh igneous rocks. However, it had a more pronounced influence on the formation of other UDMA intrusions, such as those in Kashmar and Niyasar, e.g., [40,110].

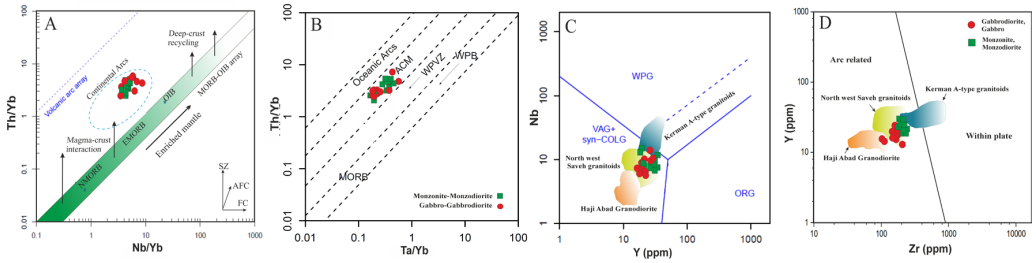


Figure 14. Geochemical tectonic discrimination diagrams for plutonic rocks from northeast Saveh: (**A**) Th/Yb vs. Nb/Yb diagram [111]; (**B**) Th/Yb vs. Ta/Yb diagram, after [112]; (**C**) the northeast Saveh samples in the Nb (ppm) vs. Y (ppm) from [71]; (**D**) Y vs. Zr geo-tectonic discrimination diagram from arc-related granite and for within-plate granite (after [101]. Abbreviations: WPG = within-plate granite (A-type), VAG = volcanic arc granite (I-type), ORG = oceanic ridge granite, syn-COLG = syn-collisional granite (S-type).

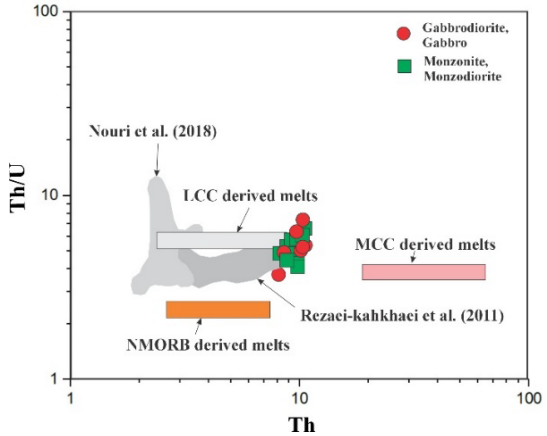


Figure 15. Th/U vs. Th (ppm) plot. The plutonic samples from northeast Saveh mainly group in the region associated with magma derived from continental crust rather than in the area related to N-MORB-derived magma [105]. LCC: lithospheric continental crust, MCC: microcontinent crust. Northwest Saveh data from [40,41].

5.2. Characteristics of Mantle Source and Nature of Magma

The composition of the mantle wedge is altered by the inclusion of slab components during subduction [113]. The Yb vs. La/Yb plot (Figure 4D) suggests that these intrusive rocks do not display an adakite signature, indicating that slab melt did not contribute to the magma generation.

Using trace element ratios such as Ba/La, Ba/Th, and Ce/Pb, it is possible to evaluate the influence of fluids derived from the altered oceanic basaltic crust (low-temperature aqueous fluids) and of sedimentary melts (sediment components) on the mantle wedge (geo-)chemistry [114]. Ref. [115] shows that the Ce/Pb ratio is primarily controlled by the proportion of sedimentary melt to fluid components. Consequently, subducted sediment melts produce higher Ce/Pb ratios, whereas fluid components lead to lower ratios.

As [116] shows, high Ba/Th ratios in melts suggest the contribution of slab-derived fluids, whereas high levels of Th in melts indicate the influence of pelagic sediment melt in the magma source. The Th/Yb vs. Sr/Nd plot [117] reveals the influence of fluids released from the subducting slab on the composition of the parent magma (Figure 16A). The increase in Sr/Nd values, along with the relatively stable Th/Yb ratio in the region's samples, suggests that the released fluids play a dominant role in mantle metasomatism, while melting processes have a less significant influence.

As shown in Figure 16B,C, the plots of Ce/Pb vs. Ba/La and Th vs. Ba/Th demonstrate that fluid components and melt were involved in the subduction process of the northeast Saveh rocks.

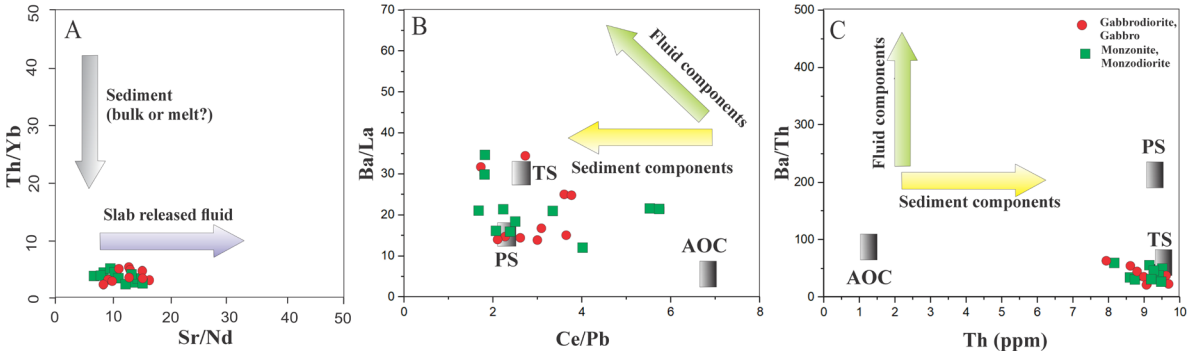


Figure 16. (**A**) Th/Yb vs. Sr/Nd diagram. (**B**) Ce/Pb vs. Ba/La diagrams for plutonic rocks from northeast Saveh. (**C**) The Th (ppm) vs. Ba/Th plot, showing contribution of sediment and fluid. (AOC): altered oceanic crust, (TC): terrigenous, and (PS): pelagic sediments.

To evaluate the potential sediment incorporation, we employed the Th/Yb vs. Nb/Yb plot [118], which exclusively utilizes fluid–immobile elements. The analyzed samples predominantly plot away from the MORB array, possibly indicating a sedimentary component of more than 4% wt.% (Figure 17A), which is consistent with the negative Nb anomaly observed in Figure 7.

The inferred primary melts at northeast Saveh have $Na_2O > K_2O$ and suggest melting of four-phase peridotites (Supplementary Table S1). Phlogopite and amphibole are some of the most prevalent volatile-bearing minerals and act as the major storage sites for large-ion lithophile elements in the mantle. Useful information can be obtained from trace elements regarding the role of hydrous mineral phases in the melting process.

Ref. [119] states that while Ba and Rb are compatible with phlogopite and biotite, and Ba, Rb, and Sr are moderately compatible with amphibole, melts in equilibrium with phlogopite exhibit higher Rb/Sr ratios (>0.1) and lower Ba/Rb ratios (<20) compared to melts derived from amphibole-bearing sources. As shown in Figure 17B, the data reveal the presence of both phlogopite and amphibole in the mantle source area. Ref. [120] presents an

experimental model in which an ascending aqueous fluid infiltrates the initially dry mantle wedge, precipitating amphibole. As the fluid continues rising, trace elements either incorporate into the amphibole or induce melting in hotter regions, forming an amphibole-rich zone enriched in incompatible elements (excluding Ta and Nb). Consequently, the amphibole in northeast Saveh samples is interpreted as a product of mantle source enrichment during subduction.

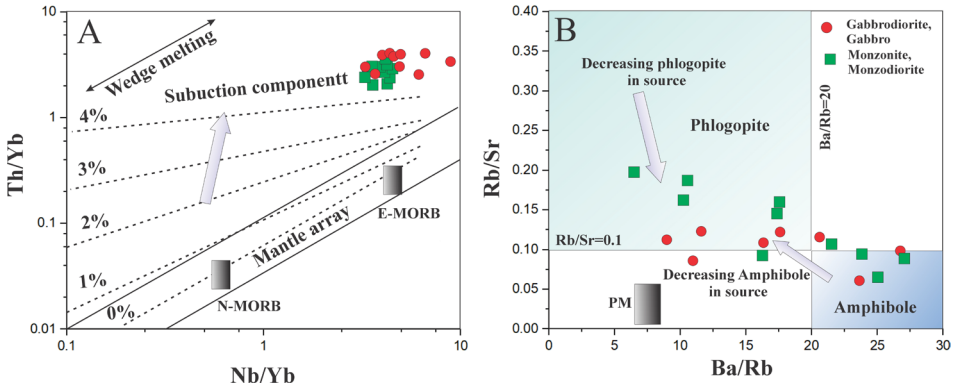


Figure 17. (**A**) Th/Yb vs. Nb/Yb ratios of plutonic rocks from northeast Saveh (the studied samples), after [118]. (**B**) Ba/Rb vs. Rb/Sr schematic arrows suggest phlogopite and amphibole controls during partial melting, after [119].

The flat chondrite-normalized HREE patterns (Figure 7A) in the northeast Saveh rocks rule out an eclogite source because the significant reduction in HREEs is caused by partial melting of eclogite with residual garnet [109]. As noted by [121], La/Sm, Sm/Yb, and La/Yb are ineffective in processes like fractional crystallization or partial melting, where pyroxene and feldspar are the primary minerals involved. In contrast to the incompatible behavior of La and Sm, Y is compatible with garnet. This compatibility results in pronounced fractionation of Sm/Yb and La/Sm ratios at lower degrees of melting. On the other hand, when lower-degree melting occurs within the spinel stability field, La/Sm ratios show slight fractionation, whereas Sm/Yb ratios remain almost unchanged. Given the absence of a discernible correlation between MgO and the REE fractionation patterns (Sm/Yb, La/Sm, and La/Yb) in the northeast Saveh intrusive suite, it can be inferred that these trace element ratios are largely decoupled from fractional crystallization processes, thereby providing robust constraints on the mantle source characteristics. Figure 18A presents the La versus La/Sm diagram [122], which emphasizes that variations in the La/Sm ratios are reflective of differences in the degree of partial melting within the source regions. The observed variability in these ratios indicates that partial melting processes play a critical role in shaping the geochemical characteristics of the intrusive bodies in northeast Saveh.

Additionally, the La/Sm vs. Sm/Yb diagram [122] in Figure 18B suggests that the magmas were derived from a metasomatized mantle, with up to 10% partial melting of spinel lherzolite. Magmatic rocks from northeast Saveh, similar to those in the central UDMA, exhibit relatively low $(Dy/Yb)_N$ ratios, ranging from 1.9 to 2.2. The lack of systematic variation from the Eocene to the Miocene indicates the partial melting of spinel lherzolite. The transition from garnet peridotite to spinel is suggested to occur at a mantle depth of approximately 75–80 km (as indicated by the mantle solidus) [123]. This suggests that the magmas from northeast Saveh were likely formed at depths of less than 80 km.

In addition, low $(La/Sm)_N$, $(Sm/Yb)_N$, and Sm/Yb ratios (Figure 18C,D) indicate a magma with a low garnet contribution in its source that formed northeast Saveh samples. This observation is supported by the enrichment of Ce/Sm (average 8.4), which is significantly higher compared to Sm/Yb (average 1.6). This pattern occurs when garnet is absent

in the source, implying that Ce has entered the mineral phase. Given the weak fractionation between MREEs and HREEs, likely due to the minimal presence or scarcity of residual garnet in the mantle composition, it can be deduced that their magmas originated from the melting of spinel lherzolite. Moreover, the low CaO/Al_2O_3 ratios (0.23–0.63), the HREE enrichment exceeding the chondrite-normalized values 10 times, and the relatively flat MREE-HREE patterns in our samples suggest that garnet was not present in the deduced mantle source. The formation of the northeast Saveh plutonic rocks is likely linked to the melting of peridotite at relatively shallow levels (<80 km). This interpretation is reinforced by the generation of the northeast Saveh parental magma within the stability range of spinel–lherzolite and the transition depth between spinel and garnet at the peridotite melting point (approximately 75–80 km), as outlined by [124].

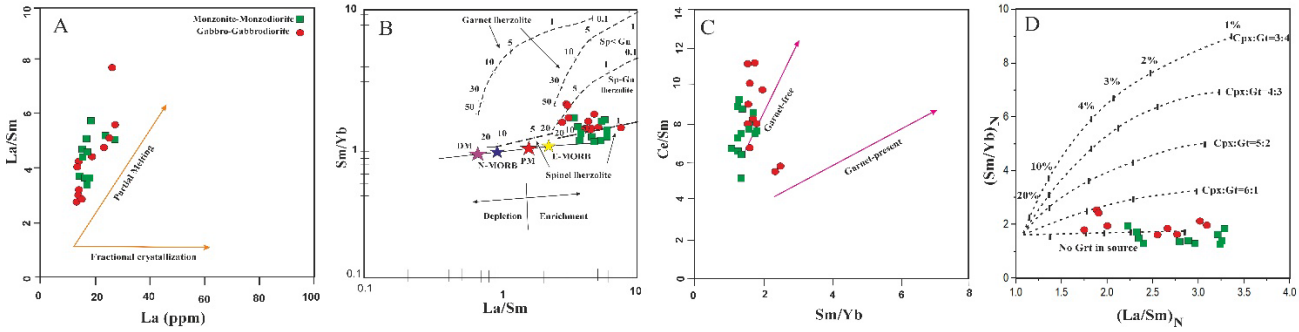


Figure 18. Diagrams illustrating the magmatic nature of plutonic rocks from northeast Saveh: (**A**) determination of partial melting process in La/Sm vs. La plot [122]; (**B**) Sm/Yb vs. La/Sm plot displays the melt curves derived from fractional and batch melting equations [125]; (**C**) determination of absence or presence of garnet at source in Sm/Yb vs. Ce/Sm [126]; (**D**) $(La/Sm)_N$ vs. $(Sm/Yb)_N$ plot—trends of batch melting for different clinopyroxene/garnet ratios [127].

5.3. Composition of Minerals

The low TiO_2 content in the northeast Saveh pyroxenes may reflect either their formation in a subduction-related tectonic setting or the influence of magmatic differentiation processes, which tend to reduce TiO_2 levels in arc magmas [128]. The magnesium number (Mg#) is a crucial indicator used to examine the compositional variations of pyroxenes. The formula for Mg# is expressed as $Mg\# = Mg/(Mg + Fe^{2+})$. Clinopyroxenes vary from 0.69 to 0.82, while for orthopyroxenes, the range is from 0.5 to 0.65. Figure 19A compares the Al_2O_3 content and Mg number, illustrating the compositions of clinopyroxenes in northeast Saveh. The figure also displays the respective fields for arc-related crustal pyroxenes and arc-related mafic cumulates, with orthopyroxenes trending toward more evolved arc-related mafic cumulates. Additionally, the Fe vs. Si content confirms the subduction tectonic setting (Figure 19B). The F1 vs. F2 (calculations in Supplementary Table S3) bivariate plot [129] effectively distinguishes the pyroxenes of intraplate volcanic rocks from other types. The separation of WPT magma from VAB magma is also well-demonstrated; however, considerable overlap between VAB and VAB-OFB is observed. The results of sample analysis in this diagram (Figure 19C) indicate that the volcanic samples of the region are situated within the realm of volcanic arcs. Ref. [130] proposes the Al^{IV} + Na vs. Al^{VI} + 2Ti + Cr bivariate plot (Figure 19D) based on the substitution of trivalent cations in the octahedral site in clinopyroxene. The composition of clinopyroxene falls within the high oxygen fugacity range. This feature suggests the crystallization of clinopyroxene under high oxidation conditions. The high water content in the pyroxene samples is consistent with high fugacity values. The water content and oxygen fugacity themselves indicate a subduction setting. In the TiO_2 vs. Al_2O_3 plot for pyroxenes [131], the clinopyroxenes mainly group in the low-pressure

field (Figure 19E). In the Al_2O_3 vs. Mg# bivariate plot presented by [132], orthopyroxene deviates from the Al_2O_3 enrichment trend, displaying instead a pattern consistent with low-pressure differentiation. This behavior, attributed to its comparatively low Al_2O_3 content, indicates that magma crystallization likely occurred in a shallow magma chamber at upper crustal depths under low-pressure conditions (Figure 19F). The low Al_2O_3 content in orthopyroxene [132] and the low Cr_2O_3 content in clinopyroxenes (<0.75 wt%; [133] also suggests that the source magma of the monzonitic and gabbroic rocks crystallized under low-pressure settings. In addition, the chemical composition of pyroxene is valuable for determining the physical conditions during magma crystallization. Ref. [134] also proposes the XPT vs. YPT bivariate plot (calculations in Supplementary Table S3) to determine the temperature and pressure at which pyroxene crystallization occurs. Based on this, the crystallization pressure of the two groups of pyroxenes in the studied rocks is less than 2 kb, and the average crystallization temperatures of clinopyroxene range mostly from 1150 °C to 1200 °C, according to [134], and from 1100 °C to 1150 °C in orthopyroxene (Figure 19G,H).

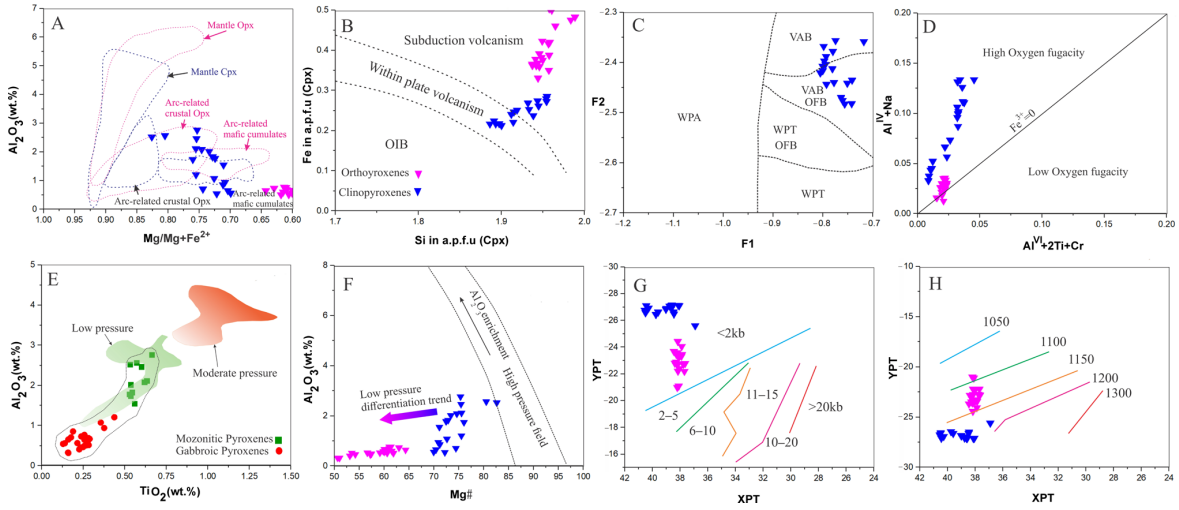


Figure 19. Pyroxene chemistry diagrams of plutonic rocks from northeast Saveh. (**A**) Al_2O_3 vs. Mg number for clinopyroxene and orthopyroxene (reference fields from [135] and references therein); (**B**) tectonic classification diagrams [136]. using Fe vs. Si content in clinopyroxene and orthopyroxene; (**C**) using clinopyroxene composition to display the tectonic environment of northeast Saveh rocks in the F1-F2 diagram [129]; (**D**) determination of oxygen fugacity of clinopyroxene and orthopyroxene precipitation settings [130]; (**E**) clinopyroxene TiO_2 vs. Al_2O_3 diagram [131]; low and moderate pressure fields, after [133]; (**F**) orthopyroxene and clinopyroxenes Mg# vs. Al_2O_3 diagram [133]; (**G**) the pressure determination diagram for clinopyroxenes [134] indicates that the formation pressure of clinopyroxenes and orthopyroxene in the northeast Saveh is <2 kb; (**H**) the pressure temperature diagram using Ypt and Xpt parameters [134] indicates that the precipitation temperature of orthopyroxene and clinopyroxenes is between 1100 °C and 1200 °C.

5.4. Crustal Contamination Signatures

Crustal contamination alters the radiogenic isotope ratios and major and trace element compositions of the mantle-derived magmas, e.g., [137,138]. When mafic and intermediate magmas interact with continental crustal materials, they typically undergo geochemical modifications. These changes often manifest as a depletion in Ta, Ti, Nb, and P, with enrichment in LREEs and Th, e.g., [139–143]. Both groups of mafic and intermediate magmatic rocks in northeast Saveh show similar patterns to those mentioned above in primitive mantle-normalized multi-element diagrams (Figure 7B).

The geochemical consistency of Lu and Yb suggests that Lu/Yb ratios are robust indicators, minimally influenced by processes like partial melting or fractional crystallization.

Magmas that originate from the mantle are distinguished by relatively low Lu/Yb ratios, generally ranging from 0.14 to 0.15 [82]. In contrast, according to [140], the continental crust, with average Lu/Yb ratios of 0.16–0.18, is enriched in Lu compared to Yb. The Lu/Yb ratios in the northeast Saveh plutonic rocks display a range of 0.10 to 0.23, suggesting that they originate from both mantle and continental crust sources.

Additionally, according to [144], the observed narrow range of Nb/Y ratios and the wide range of Rb/Y ratios suggest possible crustal contamination.

Ta and Nb are also highly sensitive to crustal contamination. Mantle-derived magmas, which may interact with continental crustal rocks during their ascent, often display negative Ta and Nb anomalies in spider plots [83,145].

The long-term subduction process likely resulted in the substantial contamination of the mantle source region. The involvement of fluids released from the hydrated subducted slab and associated sedimentary rocks, as well as melts generated by the partial melting of the slab, likely played a key role in modifying the mantle source composition and triggering magma generation [146] (Figure 20A).

The northeast Saveh plutonic rocks exhibit geochemical signatures that are consistent with a magmatic history involving multiple processes, including assimilation, fractional crystallization, and crustal contamination, as demonstrated by incompatible element ratio diagrams (Figure 20B). The interaction with older magmatic rocks likely resulted in the observed increase in K_2O/Na_2O, Rb/Zr, and Sm/Nd ratios.

The wide range of Hf isotopic composition in zircons with identical ages in a cluster rules out basic fractional crystallization and suggests the involvement of alternative processes, such as the incorporation of the continental crust. Consequently, the detected Hf heterogeneity in the zircons from northeast Saveh rocks reflects the composition of the melt derived from the mantle and primary crustal materials (AFC) (Figure 20C).

This finding is consistent with the significant presence of inherited zircons in the samples, as previous studies, e.g., [8,19,37,40], have reported inherited zircons with elevated Sr and Nd isotope ratios in magmatic rocks from the UDMA. These observations suggest that the mafic parent magmas experienced moderate degrees of crustal contamination in Ardestan, Eshtehard, Saveh, and Kahak (the central UDMA).

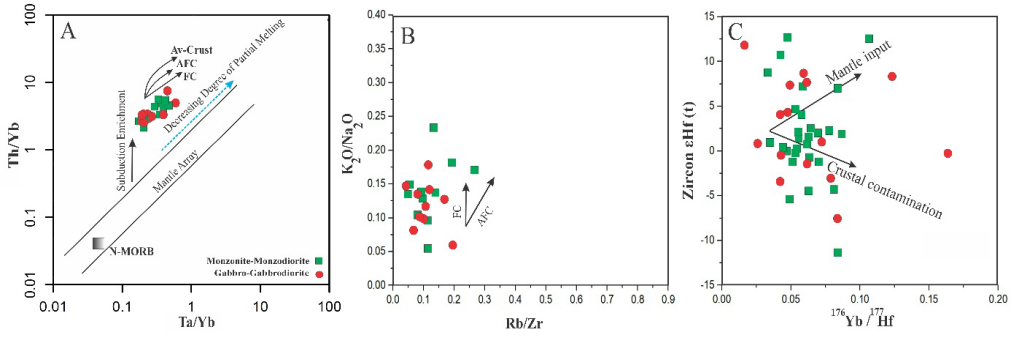


Figure 20. (**A**) Ta/Yb vs. Th/Yb discrimination diagrams [71] show that northeast Saveh plutonic rocks deviate from the mantle array, suggesting crustal contamination or subduction-related metasomatism; (**B**) K_2O/Na_2O vs. Rb/Zr ratios plots for the northeast Saveh plutonic rocks; (**C**) variations in the ratio of $^{176}Yb/^{177}Hf$ vs. εHf for northeast Saveh zircons illustrate mantle-derived magma addition and crustal contamination effects.

5.5. Fractional Crystallization

Intermediate to acidic magmas typically form through the fractional crystallization of mafic magmas or the partial melting of crustal material [147]. As shown in Figure 6, the concentrations of Al_2O_3, CaO, MgO, TiO_2, Fe_2O_3, and P_2O_5 decrease steadily as the SiO_2 content increases. The negative correlations between Al_2O_3, MgO, Fe_2O_3, TiO_2, and

SiO_2 suggest that clinopyroxene, olivine, hornblende, magnetite, and ilmenite, respectively, crystallized early and were removed from the magma. Additionally, the decrease in Al_2O_3 and CaO aligns with the early fractionation of Ca-rich plagioclase. Furthermore, the reduction in CaO concentration suggests the removal of calcium-bearing minerals like plagioclase, hornblende, and clinopyroxene, which are present in northeast Saveh rocks.

The positive correlation between SiO_2 and K_2O (Figure 6F) further supports the assumption that K-feldspar remained unaffected by fractionation. According to [148], the fractionation of biotite and K-feldspar is expected to reduce Ba concentrations in the remaining melt. Increasing K_2O suggests that the fractionation of a K-bearing phase, such as biotite, was not significant.

The TiO_2 and P_2O_5 abundances exhibit a nearly linear positive trend in the northeast Saveh rocks (Figure 6), indicating that P and Ti, likely hosted in apatite and titanomagnetite, respectively, have persisted in the mineral assemblage until the final stages of crystallization. Strontium is incompatible with clinopyroxene and compatible with plagioclase. Consequently, the fractionation of plagioclase leads to a negative correlation between the Sr concentration and Si content (Figure 21A) in the resulting minerals.

Figure 21B shows a positive correlation between Sr and MgO up to a critical point of 3.4 wt.% MgO (equivalent to 55 wt.% SiO_2), beyond which the trend becomes negative. This indicates that clinopyroxene played a key role in controlling the depletion of MgO, CaO, and Fe_2O_3 in rocks with MgO concentrations above 3.4 wt.%.

The low Dy/Yb ratios in the study samples, combined with a decreasing Dy/Yb ratio as the silica content increases (Figure 21C), strongly suggest that the fractionation of amphibole, without garnet involvement, is the primary mechanism responsible for the evolution of northeast Saveh magmas. Additionally, although the trend in Rb/Sr ratios with decreasing Sr concentrations in Figure 21D is subtle and not immediately apparent, a more detailed analysis reveals slight systematic variations. When considered alongside other geochemical data, these variations support the interpretation that clinopyroxene fractionation contributes to the development of mafic magmas, while the cumulative effects of hornblende and plagioclase fractionation are important in the evolution of felsic magmas, e.g., [149]. As illustrated in Figure 21E, a distinct decline in CaO/Al_2O_3 ratios with a decrease in SiO_2 levels suggests the fractionation of clinopyroxene (alongside olivine).

The approximate reduction in Sr concentrations with increasing Rb/Sr ratios in Figure 21D suggests that plagioclase could be a major crystallizing phase controlling the fractionation of REEs. The influence of plagioclase on these rocks becomes more evident when considering trace element trends rather than Na_2O trends. Since Eu and Sr substitute for Na and Ca in plagioclase (unlike in clinopyroxene), as shown in (Figure 21A), Sr concentrations decrease with increasing silica content. Conversely, Eu concentrations initially increase with increasing silica up to ca. 54 wt.% silica, after which they decrease (Figure 21F).

While plagioclase fractionation could contribute to the observed trends in magmas with more than 54 wt% SiO_2, the potential influence of crustal melt incorporation must also be considered, as it may obscure fractional crystallization signatures in whole-rock compositions. Moreover, the reduction in Eu/Eu* ratios as SiO_2 concentrations rise and the presence of negative Eu anomalies can indicate feldspar fractionation. The increased partitioning of Eu observed throughout magmatic development indicates conditions of low fO_2.

Figure 21G shows an approximate positive correlation between Sr and Eu/Eu, which could suggest plagioclase fractionation in the northeast Saveh rocks with SiO_2 concentrations exceeding 55 wt.%. However, this pattern is not strongly evident, and alternative processes, such as crustal melt incorporation, may also have influenced the observed geochemical trends. The constant Ta/Nb ratio (Figure 21H) suggests that magnetite also un-

derwent fractionation in the northeast Saveh magmas. The La/Yb vs. La ratio (Figure 21I) reveals that the diverse compositions of the northeast Saveh plutonic rocks are best explained by fractional crystallization rather than partial melting.

This is supported by the TiO_2 vs. Zr plot (Figure 21J), which shows that samples experienced crustal contamination throughout fractional crystallization. Therefore, the integrated process of assimilation and fractional crystallization (AFC) should be taken into account as well.

A comparison of the REE patterns in northeast Saveh magmatic rocks with the Rayleigh REE-FC modeling diagrams from Sabzevar Eocene volcanic rocks in NE Iran [58,60], Saveh [40], and Eshtehard [8] (Figure 21K,L), reveals nearly identical REE trends. This comparison suggests that the fractional crystallization in these rocks was less than 20%.

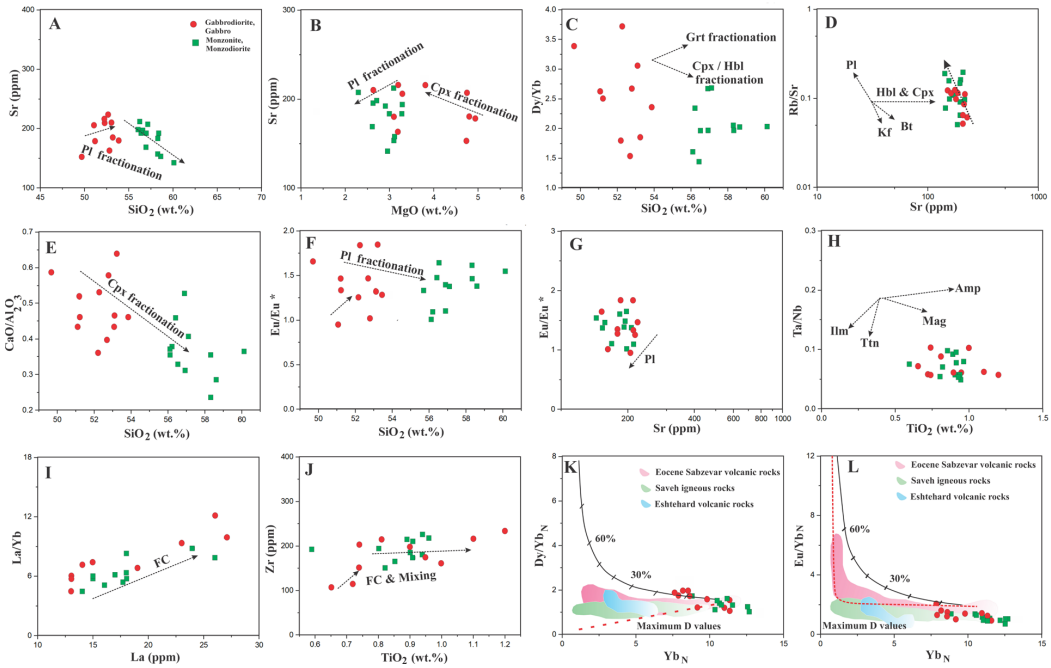


Figure 21. Diagrams showing the petrogenetic processes of the northeast Saveh Plutonic rocks. (**A**) SiO_2 vs. Sr; (**B**) MgO vs. Sr; (**C**) SiO_2 vs. Dy/Yb; (**D**) Rb/Sr vs. Sr; (**E**) SiO_2 vs. CaO/Al_2O_3; (**F**) SiO_2 vs. Eu/Eu*; (**G**) Sr vs. Eu/Eu*; (**H**) TiO_2 versus Ta/Nb; (**I**) The La/Yb vs. La plot, which indicates the varying compositions of the northeast Saveh rocks are aligned with fractional crystallization; (**J**) The TiO_2 vs. Zr plot, according to [150], demonstrates that the samples follow the trend of fractional crystallization. (**K**,**L**) Rayleigh REE–fractional crystallization modeling, after [60].

5.6. Multi-Stage Tertiary Magmatism in Northeast Saveh

Analysis of the samples reveals the presence of several age groups or zircon populations (Figure 22). To ensure the geological relevance of the obtained U-Pb dates, the data were assessed for potential Pb loss, open system behavior, and analytical uncertainties. Singular ages or discordant data points were excluded, and the remaining dataset was validated.

Low positive εHf values (0–5) suggest evidence of crustal contamination or the presence of xenocrystic zircon, whereas high positive εHf values (>5), indicate mantle-derived magma with no/or minimal crustal contamination [151,152].

According to [153], crustal contamination during magmatic evolution results in negative εHf values in zircon. Therefore, the presence of negative εHf values in the northeast Saveh samples indicates crustal contamination, as was also evident from whole-rock geochemical studies. Based on [97], the involvement of Mesoproterozoic continental crust in the Ediacaran–Cambrian basement of Iran is indicated by the $^{176}Hf/^{177}Hf$ values of

some inherited zircons in this study, which correspond to TDM ages ranging from 0.5 to 1.5 billion years. Additionally, the development of a Cenozoic continental arc over the Ediacaran–Cambrian crust is reflected by Eocene and Miocene zircons, with TDM ages ranging from approximately 230 to 900 Ma.

The most ancient zircon age obtained in this study (2.8 Ba) aligns with the ages of inherited zircons from the Archaean, Paleoproterozoic, and pre-Neoproterozoic periods, as documented in prior research in Iran [7,63,99,154] and the Arabian Nubian Shield [48]. This correspondence in age supports the theory of a concealed, older crustal layer beneath the upper crust of Iran [99].

Fragments of Cadomian and Avalonian crust, which currently form the basement of Paleozoic orogenic belts (i.e., Ediacaran–Early Cambrian; 500–600 Ma) in Europe, eastern North America, Turkey, and Iran, have been documented by several studies, e.g., [33,155–158].

Therefore, it can be said that based on the age range of the inherited zircons (ca. 544–713 Ma) analyzed in this study, they originated from the basement rocks of Iran. Specifically, these basement rocks comprise felsic plutonic and volcanic rocks from Neoproterozoic–Early Cambrian, as documented in previous research, e.g., [48,63,159,160].

The occurrence of inherited zircons with U-Pb ages between 252 and 476 Ma points to the preservation of the magmatic history of the active continental margin of the extinct Proto-Tethys Ocean, e.g., [161]. This is similar to other granitic plutons related to Gondwanan collisions along the northern margin of Africa, through Turkey and Iran, to the Himalayas.

The presence of several inherited zircons in the studied samples, dated between approximately 75 to 197 Ma, can be explained by the Mesozoic magmatism in Iran, such as Alborz Triassic alkaline basaltic rocks [162], the Jurassic magmatic rocks of the Sanandaj–Sirjan zone [163], Central Iran (Nain–Baft plagio-granites; [164], I-type granites and gabbrodiorites from Northwest Iran [47], and late Cretaceous volcanism in the northern UDMA [165]. Additionally, the occurrence of Cretaceous-inherited zircons (∼146 to 76 Ma) within the study samples can be linked to a Late Cretaceous magmatic event.

The isotopic characteristics of these Cretaceous zircons, particularly their Hf isotope signatures derived from a depleted mantle and notably positive εHf(t) values (∼+10), are similar to those observed in the Cretaceous Jiroft plutons in the southeastern UDMA [166]. This suggests a period of Mesozoic magmatism spanning from the Triassic to the Late Cretaceous, which generated zircons with Hf isotopes originating from a depleted mantle and εHf(t) values ranging from −7.4 to +12.5 (Figure 12A,B).

Previous studies, e.g., [9], indicate a short quiescence, ca. 15 Ma, in the UDMA from around 72 to 57 Ma. However, the presence of zircons with an age range of ca. 55 to 63 (60.4 ± 0.8) Ma in this study (Figure 10C) suggests a shorter period of quiescence (∼10–12 Ma) in the UDMA.

The formation of plutonic rocks in northeast Saveh with Late Eocene ages (∼ 40–47 Ma, Figure 10D) is in agreement with the major magmatic events documented in the central UDMA, e.g., [8,9,31,35,37,40,57,167].

The occurrence of zircons with ages ranging from ca. 23 to 18 Ma (Figure 10E) aligns with the timing of Early Miocene magmatism within the UDMA (e.g., Tafresh; [168], Kashan; [21], Eshtehard; [8]; Kahak [167]. These zircons are considered to have crystallized during the final stages of low-angle subduction and just before the collision of the Arabian and Eurasian lithospheric plates.

Evidence exists of small magmatic pulses ca. 11 to 8 Ma (e.g., ultrapotassic rocks in Saray, NW Iran [47], volcanic rocks in northeastern Anatolia [54], Ardestan and Tafresh Late Miocene zircons and Early Miocene plutons [37] and Eshtehard volcanic rocks [8] located in the central UDMA and interpreted in relation to the collision between the Arabian–Eurasian plates).

A geodynamic model by [54] suggests that from around 6.5 Ma, significant magmatism and volcanic activity occurred in the Caucasus–Iran–Anatolia region. This includes basaltic

rocks in northeastern Anatolia and adakitic ignimbrites from the Sabalan and Sahand in NW Iran [169,170].

Zircons from monzonitic rocks (12–5 Ma) with predominantly positive εHf(t) values, along with those from gabbroic rocks (11–2.5 Ma), mark the final magmatic stages until about 2.5 Ma and can be recognized as the youngest and final magmatic pulls in the central part of the UDMA. Magmatic activity younger than ~12 Ma in the central UDMA and northwestern Iran reflects a gradual decline from the Late Miocene to the Pliocene, likely due to a shift in the subduction angle.

According to [171], zircons younger than ~12 Ma in the Eocene northeast Saveh rocks may originate from the widespread infiltration of zircon-bearing fluids through intergranular networks in large channels. These fluids can transport zircons from both later and earlier magmatic phases, while subsequent reheating and recrystallization may erase clear intrusive textures, leaving only subtle microscopic evidence [171].

Similarly, the Hf isotopic variation in Tertiary zircons (−5.5 to +11.5) likely reflects hafnium heterogeneity. As [98] suggests, this variability may arise from the mixing of zircon-saturated mantle melts with diverse isotopic end-members and crustal materials, followed by homogenization after zircon dissolution. This complex history, indicating the involvement of both mantle and primary crustal components, is consistent with the abundance of inherited zircons and whole-rock geochemical data (Figure 23).

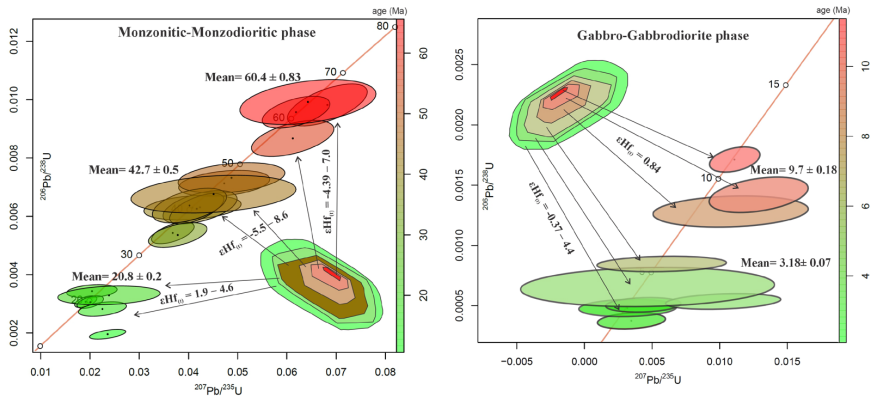


Figure 22. A schematic representation of zircon age clusters, along with the average measured $\varepsilon Hf_{(t)}$ at each stage for plutonic rocks from northeast Saveh.

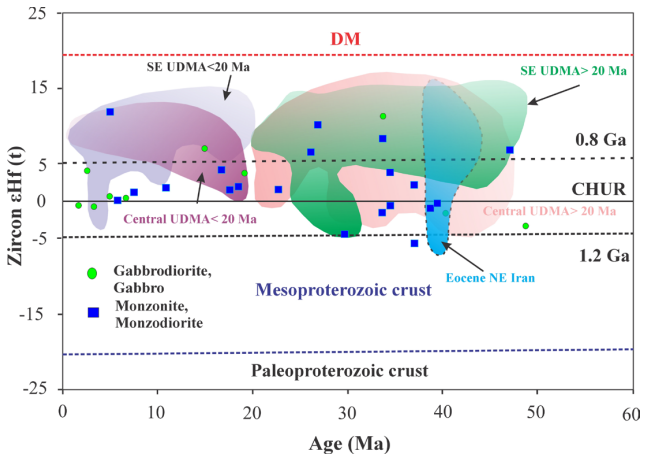


Figure 23. Variations in U-Pb age versus εHf in UDMA and the positions of samples from plutonic rocks of northeast Saveh relative to them. Modified after [9].

5.7. Geodynamic Evolution

In the central UDMA, arc magmatism re-emerged around 60 Ma, marking its role as a continental margin arc following a prolonged hiatus in magmatic activity (Figure 24A,B). Eocene calc-alkaline magmatism in the central UDMA implies a subduction angle potentially less than 15.7 degrees, and according to [57], the estimated subduction angle of the Neo-Tethyan oceanic crust under Central Iran ranges between 29.7 and 15.8 degrees.

This lithospheric thinning (in association with the Arabian–Iranian collision [172] facilitated the ascent of asthenospheric melts into shallower zones, such as the mantle wedge.

Several studies propose that slab rollback initiated in the Early Eocene reached its peak between the mid-Eocene and early Miocene (~47–15 Ma [8,35,37,40,44,49,173,174]. Geochemical, isotopic, and radiometric evidence suggest that this process was later succeeded by the initiation of the collision involving Arabia around 15–11 Ma [44,147].

Ref. [44] demonstrates that the depth at which partial melting occurred remained consistent over time, indicating stable crustal and lithospheric thicknesses spanning 50 to 18 Ma. Magmatism in the central UDMA resumed around 60 Ma, forming a continental margin arc after a prolonged dormancy, attributed to the flattening of the Cretaceous Neo-Tethyan slab between the UDMA and SSZ [28,175]. This study corroborates these findings, with an age determination of 60.4 ± 8 Ma supporting this study's interpretation.

At the onset of the Paleocene, the subducting slab shifted from a low-angle, low thermal gradient (<10–15 km) configuration with significant lithospheric dehydration to a steeper angle beneath the UDMA, following a Cretaceous flat-slab phase. During the Paleocene–Middle Eocene, continued subduction led to slab rollback—where gravitational sinking outpaced plate convergence—allowing the asthenospheric mantle to penetrate the gap between the slab and mantle wedge. The rising asthenosphere, driven by rollback-induced lithospheric stretching and thinning, heated the mantle wedge, reducing pressure and triggering partial melting in metasomatic regions (Figure 24C).

After the Paleocene, the magmatic activity expanded, with an initial phase of magmatism occurring between the Early Eocene (54.7 ± 3.1 Ma) and the Late Eocene (37.3 ± 1.2 Ma) [28]. The primary magmatic phase in northeast Saveh, dated to the Middle Eocene (42.7 ± 0.5 Ma), aligns with this period of heightened activity (Figure 24D).

Oligocene magmatic activity was considerably less extensive compared to the Eocene and is absent in the northeast Saveh region and its vicinity (Figure 24E) (this study, [19,20,167]. A phase of magmatic inactivity from the Oligocene to the Early Miocene has been attributed to the collision of the Arabian and Eurasian plates during the Oligocene–Miocene and Late Eocene intervals [27].

Nonetheless, some research indicates that magmatic–volcanic activity persisted during both the Eocene and Oligocene, spanning approximately 55 to 25 Ma in the central UDMA [31,32,176].

Also, in this study, a distinct magmatic pulse characterized by gabbroic composition and age clusters of ~10 and 3 Ma was identified (Figure 24F).

This pulse could correspond to the concluding stages of slab steepening related to continental subduction, which facilitated the upward movement of the mantle wedge above the slab. This process induced significant partial melting, giving rise to magmatic pulses at ~42 Ma, 20 Ma, and <10 Ma.

Magmatic gaps following successive magmatic episodes occur when the subducting slab steepens, which reshapes the asthenospheric mantle wedge and heats it sufficiently to trigger arc magmatism [177]. Subducting slabs are thought to flatten during periods of magmatic inactivity, displacing asthenospheric material from the gap between the slab and the overlying plate. This displacement deprives the magmatic zone near the subduction area of its primary source, causing magmatic activity to cease [178]. However, confirming

this model for the central UDMA remains difficult without detailed insights into key magmatic and tectonic factors, such as the convergence rate, slab angle, density, and seismic evidence.

Based on our data, the Paleogene–Neogene intermediate to mafic magmatism in northeast Saveh likely resulted from asthenospheric ascent due to slab rollback, which led to the slight melting of subducting sediments. This melting likely occurred via the dehydration of the ancient lithospheric mantle or mafic lower crust during the secondary subduction of the Arabian plate beneath the Iranian block after their middle Eocene collision. The rising asthenosphere caused thermal perturbations that partially melted the lower continental lithosphere, allowing the resulting magma to ascend through crustal fractures. Geochemical evidence—such as LILEs (e.g., Ba), elevated Th/Nb and Th/Yb ratios, and low (Dy/Yb)N ratios (0.9–2.4), indicating garnet absence—supports the involvement of subducted sediments and suggests melting at shallower depths (within the spinel stability zone).

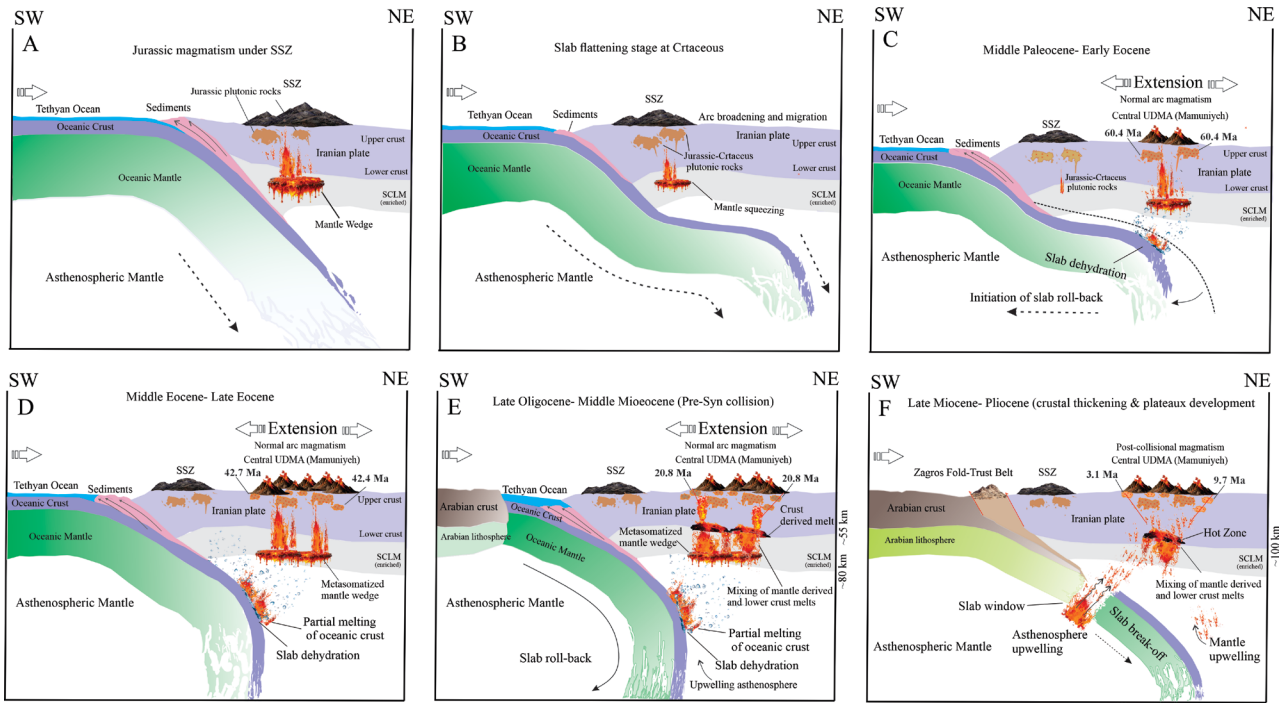


Figure 24. A schematic geodynamic model illustrating the formation of magmatic rocks in northeast Saveh (central UDMA). (**A**) Magmatism of Mesozoic (Jurassic) and subducting of Neo-Tethys beneath the Sanandaj Sirjan Zone (SSZ). (**B**) Subduction movement from SSZ to UDMA and slab flattening at Cretaceous. (**C**) Middle Paleocene–Early Eocene subduction of the Neotethyan oceanic lithosphere under the continental margin of the Iranian plate. (**D**) Extension of the overlying lithosphere and main magmatic pulse in central UDMA during the Middle Eocene to Late Eocene, simultaneously with slab roll-back and partial melting of the oceanic crust. (**E**) New magmatic pulses during slab rollback and partial melting of the slab in eclogite facies, following extensional tectonism, occurred from the Late Oligocene to the Middle Miocene. (**F**) Final magmatic pulses during the Late Miocene to Pliocene and asthenospheric upwelling during slab break-off.

6. Conclusions

This study of the magmatic units in the northeast Saveh (the central UDMA) allows several noteworthy conclusions based on zircon U-Pb geochronology, Lu-Hf isotopes, and geochemical data:

- The northeast Saveh magmatic rocks in the central UDMA comprise metaluminous, medium-K calc-alkaline monzonitic to gabbroic compositions;

- The intermediate to mafic magma in northeast Saveh's parental rocks originated from the partial melting of a shallow, metasomatized lithospheric mantle, likely triggered by extensional forces related to slab rollback and accompanied by localized compressional stresses. This tectonic interaction facilitated decompression melting at relatively low pressure. Additionally, while some geochemical trends suggest that magma evolution was influenced by the fractional crystallization of plagioclase, clinopyroxene, and hornblende, the scattered nature of the patterns suggests that other processes, such as magma mixing or crustal assimilation, may also have played a role;
- The magmatic rocks formed under subduction-related, low-pressure conditions (<2 kb), with 1150–1200 °C crystallization temperatures. Geochemical data suggest a metasomatized mantle source with up to 10% partial melting in the spinel–lherzolite field and sedimentary subduction inputs (>4 wt.%) and melting depths below 80 km;
- The studied zircon grains from northeast Saveh reveal a complex magmatic and tectonic history in Iran, encompassing contributions of magmatic rocks from the Mesoproterozoic to the Cenozoic. Negative εHf values indicate significant crustal contamination, while inherited zircon grains with ages ranging from the Archean to the Mesozoic suggest that these zircons may originate not only from primary magmatic sources but also from intermediate sedimentary reservoirs containing detrital zircon;
- Although previous studies indicate a brief quiescence of ca. 15 Ma in the UDMA, spanning from around 72 to 57 Ma, the presence of zircons with ages ranging from ∼55 to 63 Ma in this study suggests a shorter quiescent period of approximately 10–12 My in the UDMA;
- The dominant zircon populations in monzonitic rocks consist of crystals dated around 50 to 20 Ma. This age range corresponds to crystallization events that took place from the Early Eocene to the Early Miocene, which were probably sourced from a shared origin related to the subduction of the Neotethyan Plate beneath central Iran. The wide range of ages recorded suggests prolonged magmatic activity;
- The zircon clusters dated ∼12 to 5 Ma from monzonitic rocks characterized by predominantly positive εHf(t) values, along with zircons from gabbroic rocks aged ∼11 to 2.5 Ma, are interpreted in this study as representing the most recent magmatic stages. These stages are nearly contemporaneous with post-collisional magmatic activity observed elsewhere in the Arabia–Eurasia collision zone, including the Zagros Orogen and surrounding regions;
- The youngest and final magmatic pulses in the central UDMA, potentially extending across the entire UDMA, are dated between 5 and 2.5 Ma and identified in a cluster of zircons from gabbroic rocks.

Supplementary Materials: The following supporting information can be downloaded at: https://www.mdpi.com/article/10.3390/min15040375/s1, Supplementary Table S1: Major and trace element data for whole-rock samples from Northeast Saveh Magmatic rocks, Supplementary Table S2: The Electron Prob Microanalysis (EPMA) of the Plagioclase from Northeast Saveh samples, Supplementary Table S3: The Electron Prob Microanalysis (EPMA) of the Orthopyroxene and Clinopyroxene from Northeast Saveh samples, Supplementary Table S4: Zircon U–Pb isotopes data and ages of the Magmatic rocks from Northeast Saveh, Supplementary Table S5: Zircon Lu–Hf isotopes data and ages of the Magmatic rocks from Northeast Saveh, Supplementary File S1: Analytical methods.

Author Contributions: Conceptualization, M.G., H.Z. and U.K.; methodology, M.G. and U.K; software, M.G.; formal analysis, J.S., J.M. and J.B.; investigation, M.G., H.Z., U.K., M.U. and J.H.; resources, M.G. and U.K.; data curation, M.G., U.K. and H.Z.; writing—original draft preparation, M.G.;

writing—review and editing, U.K., H.Z. and D.R.L.; visualization, M.G., J.H. and M.U.; supervision, H.Z. and U.K.; project administration, M.G. and U.K.; funding acquisition, M.G. and U.K. All authors have read and agreed to the published version of the manuscript.

Funding: This research was partly funded (without a specific grant number) by the Ministry of Sciences, Research and Technology, Tehran, Iran, and the University of Vienna, Austria.

Data Availability Statement: The data presented in this study are available upon request from the corresponding author due to the on-going research.

Acknowledgments: This research is part of the senior author's Ph.D. study at Lorestan University, Iran, in collaboration with the University of Vienna, Austria. We sincerely appreciate the anonymous reviewers for their valuable time and insightful comments, which have significantly contributed to improving the quality of this manuscript.

Conflicts of Interest: The authors declare no conflicts of interest. The funders had no role in the design of the study; in the collection, analyses, or interpretation of data; in the writing of the manuscript; or in the decision to publish the results.

References

1. Navarrete, C.; Gianni, G.; Encinas, A.; Márquez, M.; Kamerbeek, Y.; Valle, M.; Folguera, A. Triassic to Middle Jurassic Geodynamic Evolution of Southwestern Gondwana: From a Large Flat-Slab to Mantle Plume Suction in a Rollback Subduction Setting. *Earth Sci. Rev.* **2019**, *194*, 125–159. [CrossRef]
2. Dung, P.T.; Usuki, T.; Hoang, N.; Usuki, M.; Minh, P.; Nong, A.T.Q.; Nguyen, Y.V.; Hieu, P.T. Emplacement Ages, Geochemical and Sr–Nd–Hf Isotopic Characteristics of Cenozoic Granites in the Phan Si Pan Uplift, Northwestern Vietnam: Petrogenesis and Tectonic Implication for the Adjacent Structure of the Red River Shear Zone. *Int. J. Earth Sci.* **2023**, *112*, 1475–1497. [CrossRef]
3. Xu, Y.; Zhang, H.; Santosh, M.; Tong, Y.; Luo, Z. Melt-Fluid Interaction in the Formation of Peralkaline Granite: Evidence from the Baiyinwula Intrusion, Inner Mongolia, China. *Lithos* **2023**, *454–455*, 107268. [CrossRef]
4. Chang, J.; Audétat, A.; Pettke, T. The Gold Content of Mafic to Felsic Potassic Magmas. *Nat. Commun.* **2024**, *15*, 6988. [CrossRef]
5. Benito, M.P.; Tibaldi, A.M.; Cristofolini, E.A.; Barzola, M.G.; Schwartz, J.J.; Molina, J.F.; Escribano, F.A. Dioritic to Granodioritic Calc-Alkaline Magmatism in the Sierra de Comechingones Southern Tip, Córdoba, Argentina: Tracking the Famatinian Arc into the Pampean Belt. *Int. J. Earth Sci.* **2024**, *113*, 611–633. [CrossRef]
6. Navarrete, C.; Gianni, G.; Tassara, S.; Zaffarana, C.; Likerman, J.; Márquez, M.; Wostbrock, J.; Planavsky, N.; Tardani, D.; Perez Frasette, M. Massive Jurassic Slab Break-off Revealed by a Multidisciplinary Reappraisal of the Chon Aike Silicic Large Igneous Province. *Earth Sci. Rev.* **2024**, *249*, 104651. [CrossRef]
7. Honarmand, M.; Xiao, W.; Nabatian, G.; Blades, M.L.; Collins, A.S.; Ao, S. Zircon U-Pb-Hf Isotopes, Bulk-Rock Geochemistry and Sr-Nd-Pb Isotopes from Late Neoproterozoic Basement in the Mahneshan Area, NW Iran: Implications for Ediacaran Active Continental Margin along Northern Gondwana and Constraints on the Late Oligocene Crustal Anatexis. *Gondwana Res.* **2018**, *57*, 48–76. [CrossRef]
8. Babazadeh, S.; D'Antonio, M.; Cottle, J.M.; Ghalamghash, J.; Raeisi, D.; An, Y. Constraints from Geochemistry, Zircon U-Pb Geochronology and Hf-Nd Isotopic Compositions on the Origin of Cenozoic Volcanic Rocks from Central Urumieh-Dokhtar Magmatic Arc, Iran. *Gondwana Res.* **2021**, *90*, 27–46. [CrossRef]
9. Babazadeh, S.; Furman, T.; Santosh, M.; Raeisi, D.; Choi, S.H.; D'Antonio, M. Middle to Late Miocene K-Rich Magmatism in Central Iran: Geochemical Characterization of the Post-Collision Mantle beneath the Urumieh–Dokhtar Magmatic Arc. *Chem. Geol.* **2024**, *665*, 122308. [CrossRef]
10. Mohammaddoost, H.; Ghaderi, M.; Kumar, T.V.; Hassanzadeh, J.; Alirezaei, S.; Babu, E.V.S.S.K. Geology, Mineralization, Zircon U-Pb Geochronology and Hf Isotopes of Serenu Porphyry Copper Prospect, Kerman Cenozoic Magmatic Arc, Southeastern Iran. *Ore Geol. Rev.* **2023**, *159*, 105540. [CrossRef]
11. Zou, D.; Zhang, H. Modification of Archean Lower Crust of the North China Craton by Magma Underplating during the Mesozoic: Evidence from Zircon U-Pb-Hf-O Isotopes of Granulite Xenoliths. *Gondwana Res.* **2024**, *125*, 368–377. [CrossRef]
12. Bhat, I.M.; Chauhan, H.; Ahmad, T.; Tanaka, T.; Bickle, M.; Asahara, Y.; Chapman, H.; Dar, R.A. Fate of an Oceanic Plate in the Neo-Tethys Intra-Oceanic Subduction System: Evidence from Elemental and Rb/Sr–Sm/Nd Isotopic Systematics. *Gondwana Res.* **2024**, *125*, 266–283. [CrossRef]
13. Noudeh Shiva, A.; Yann, R.; Magali, R.; Olivier, B.; Mohammad, R. Eocene High-K Magmatic Flare-up in a Context of South Dipping Subduction and Strike-Slip Tectonics: Insights from the Talysh Massif, NW Iran. *J. Asian Earth Sci.* **2024**, *264*, 106045. [CrossRef]

14. Mehdizadeh, H.; Liotard, J.-M.; Dautria, J.-M. Geochemical Characteristics of an Intracontinental Shoshonitic Association: The Example of the Damavand Volcano, Iran. *Comptes Rendus Géoscience* **2002**, *334*, 111–117. [CrossRef]
15. Khalatbari Jafari, M.; Sepehr, H.; Mobasher, K. Tectonomagmatic Evolution of the South Dehshir Ophiolite, Central Iran. *Geol. Mag.* **2015**, *153*, 557–577. [CrossRef]
16. Neill, I.; Meliksetian, K.; Allen, M.B.; Navarsardian, G.; Karapetyan, S. Pliocene-Quaternary Volcanic Rocks of NW Armenia: Magmatism and Lithospheric Dynamics within an Active Orogenic Plateau. *Lithos* **2013**, *180–181*, 200–215. [CrossRef]
17. Mohammadi, E. Sequence Stratigraphy of the Qom Formation in the Sirjan-Abadeh Region. *Stratigr. Sedimentol. Res.* **2020**, *37*, 1–28. [CrossRef]
18. Tunini, L.; Jiménez-Munt, I.; Fernández, M.; Vergés, J.; Villaseñor, A. Lithospheric Mantle Heterogeneities beneath the Zagros Mountains and the Iranian Plateau: A Petrological-Geophysical Study. *Geophys. J. Int.* **2015**, *200*, 596–614. [CrossRef]
19. Moradi, S.; Ghorbani, M.R.; Jiang, S.Y.; Christiansen, E.H. Mafic to Intermediate Composition Intrusions from the Kahak Area, Central Urumieh-Dokhtar Arc of Iran: Transition from Eocene to Miocene Intra-Arc Extensional Magmatism. *Miner. Pet.* **2021**, *115*, 445–466. [CrossRef]
20. Moradi, S.; Jiang, S.Y.; Christiansen, E.; Ghorbani, M.R. Petrogenesis of Tertiary Granitoid Rocks from East of the Bidhand Fault, Urumieh-Dokhtar Magmatic Arc, Iran: Implications for an Active Continental Margin Setting. *Lithos* **2021**, *400–401*, 106422. [CrossRef]
21. Khaksar, T.; Rashidnejad-Omran, N.; Chen, F.; Song, S.; Li, S.; Ghaderi, M. Zircon U-Pb Ages and Magmatic History of the Kashan Plutons in the Central Urumieh-Dokhtar Magmatic Arc, Iran: Evidence for Neotethyan Subduction during the Paleogene-Neogene. *Earth Sci.* **2020**, *31*, 53–68. [CrossRef]
22. Pirnia, T.; Saccani, E.; Torabi, G.; Chiari, M.; Goričan, Š.; Barbero, E. Cretaceous Tectonic Evolution of the Neo-Tethys in Central Iran: Evidence from Petrology and Age of the Nain-Ashin Ophiolitic Basalts. *Geosci. Front.* **2020**, *11*, 57–81. [CrossRef]
23. Rodríguez, E.E.; Portner, D.E.; Beck, S.L.; Rocha, M.P.; Bianchi, M.B.; Assumpção, M.; Ruiz, M.; Alvarado, P.; Condori, C.; Lynner, C. Mantle Dynamics of the Andean Subduction Zone from Continent-Scale Teleseismic S-Wave Tomography. *Geophys. J. Int.* **2021**, *224*, 1553–1571. [CrossRef]
24. Muttaqy, F.; Syuhada, S.; Nugraha, A.D.; Mori, J.; Puspito, N.T.; Supendi, P.; Rohadi, S. Lithospheric Mantle Dynamics in Central and East Java Region, Indonesia from Local Shear Wave Splitting Measurements. *J. Geodyn.* **2023**, *158*, 101998. [CrossRef]
25. Rabayrol, F.; Hart, C.J.R.; Thorkelson, D.J. Temporal, Spatial and Geochemical Evolution of Late Cenozoic Post-Subduction Magmatism in Central and Eastern Anatolia, Turkey. *Lithos* **2019**, *336–337*, 67–96. [CrossRef]
26. Berberian, M.; King, G.C.P. Towards a Paleogeography and Tectonic Evolution of Iran. *Can. J. Earth Sci.* **1981**, *18*, 210–265.
27. Omrani, J.; Agard, P.; Whitechurch, H.; Benoit, M.; Prouteau, G.; Jolivet, L. Arc-Magmatism and Subduction History beneath the Zagros Mountains, Iran: A New Report of Adakites and Geodynamic Consequences. *Lithos* **2008**, *106*, 380–398. [CrossRef]
28. Verdel, C.; Wernicke, B.P.; Hassanzadeh, J.; Guest, B. A Paleogene Extensional Arc Flare-up in Iran. *Tectonics* **2011**, *30*, 3008–3302. [CrossRef]
29. Boon, A.; Naudé, M.N.; Callegaro, S.; Monsef, I.; Rezaeian, M.; Niknam, A.; Cotton, L.J.; Roux, P.; Kriegsman, L.M.; Mason, P.R.D.; et al. Propagating Neotethys slab break-off beneath Iran following Arabia-Eurasia collision. *Lithos* **2024**, *482–483*, 107737. [CrossRef]
30. Yeganehfar, H.; Ghorbani, M.R.; Shinjo, R.; Ghaderi, M. Magmatic and Geodynamic Evolution of Urumieh-Dokhtar Basic Volcanism, Central Iran: Major, Trace Element, Isotopic and Geochronologic Implications. *Int. Geol. Rev.* **2013**, *55*, 767–786. [CrossRef]
31. Chiu, H.Y.; Chung, S.L.; Zarrinkoub, M.H.; Mohammadi, S.S.; Khatib, M.M.; Iizuka, Y. Zircon U–Pb Age Constraints from Iran on the Magmatic Evolution Related to Neotethyan Subduction and Zagros Orogeny. *Lithos* **2013**, *162–163*, 70–87. [CrossRef]
32. Ghorbani, M.R.; Graham, I.T.; Ghaderi, M. Oligocene-Miocene Geodynamic Evolution of the Central Part of Urumieh-Dokhtar Arc of Iran. *Int. Geol. Rev.* **2014**, *56*, 1039–1050. [CrossRef]
33. Shafaii Moghadam, H.; Khademi, M.; Hu, Z.; Stern, R.J.; Santos, J.F.; Wu, Y. Cadomian (Ediacaran–Cambrian) Arc Magmatism in the ChahJam–Biarjmand Metamorphic Complex (Iran): Magmatism along the Northern Active Margin of Gondwana. *Gondwana Res.* **2015**, *27*, 439–452. [CrossRef]
34. Sarjoughian, F.; Kananian, A. Zircon U–Pb Geochronology and Emplacement History of Intrusive Rocks in the Ardestan Section, Central Iran. *Geol. Acta* **2017**, *15*, 25–36. [CrossRef]
35. Babazadeh, S.; Ghorbani, M.R.; Bröcker, M.; D'Antonio, M.; Cottle, J.M.; Gebbing, T.; Carmine Mazzeo, F.; Ahmadi, P. Late Oligocene–Miocene Mantle Upwelling and Interaction Inferred from Mantle Signatures in Gabbroic to Granitic Rocks from the Urumieh–Dokhtar Arc, South Ardestan, Iran. *Int. Geol. Rev.* **2017**, *59*, 1590–1608. [CrossRef]
36. Wang, Z.; Zhao, Z.; Wan, Y.; Li, X.; Meng, Y.; Liu, D.; Mo, X.; Cong, F. The Initial Slab Rollback of Neo-Tethys Ocean: Constrain from Gongga Adakitic Rocks and Enclaves in the Late Cretaceous. *Lithos* **2023**, *440–441*, 107050. [CrossRef]

37. Babazadeh, S.; Ghorbani, M.R.; Cottle, J.M.; Bröcker, M. Multi-Stage Tectono-Magmatic Evolution of the Central Urumieh-Dokhtar Magmatic Arc, South Ardestan, Iran: Insights from Zircon Geochronology and Geochemistry. *Geol. J.* **2019**, *54*, 2447–2471. [CrossRef]
38. Amidi, S.M.; Shahrabi, M.; Navai, I. *Geological Map of Zaviyeh*; Geological Survey of Iran: Tehran, Iran, 2004; Volume 6160.
39. Moghadam, H.S.; Li, Q.L.; Li, X.H.; Chiaradia, M.; Karsli, O.; Hoernle, K.A.; Griffin, W.L. Mantle-Derived High-K Magmatic Fluxes in Northeast Iran Arc: Constraints from Zircon U–Pb–O–Hf and Bulk Rock Major-Trace Elements and Sr–Nd–Pb Isotopes. *Gondwana Res.* **2023**, *119*, 1–26. [CrossRef]
40. Nouri, N.; Azizi, H.; Stern, R.; Asahara, Y.; Khodaparast, S.; Madanipour, S.; Yamamoto, K. Zircon U-Pb Dating, Geochemistry and Evolution of the Late Eocene Saveh Magmatic Complex, Central Iran: Partial Melts of Sub-Continental Lithospheric Mantle and Magmatic Differentiation. *Lithos* **2018**, *314–315*, 274–292. [CrossRef]
41. Rezaei Kahkhaei, M.; Esmaili, D.; Francisco, C.G. Geochemical and Isotopic (Nd and Sr) Constraints on Elucidating the Origin of Intrusions from Northwest Saveh, Central Iran. *Geopersia* **2014**, *4*, 103–123. [CrossRef]
42. Amidi, M.A.; Shahrabi, M.; Navaei, Y. *1:100,000 Geological Map of Zavieh*; Geological Survey of Iran: Tehran, Iran, 2006.
43. Alizadeh, E.; Li, H.; Babazadeh, S.; Ma, C.; Förster, M.W. Late Eocene Slab Retreat, Extension, and Mantle Upwelling Inferred from Mantle Signatures in Potassium-Rich Magmatism in NE Iran. *Int. Geol. Rev.* **2023**, *65*, 1586–1600. [CrossRef]
44. Babazadeh, S.; Haase, K.; Ghalamghash, J.; Regelous, M.; Poujol, M.; Raeisi, D.; Zhao, M. Magmatic Evolution of the Migrating Central Urumieh–Dokhtar Arc, Iran: Implications for Magma Production. *Int. J. Earth Sci.* **2023**, *112*, 1577–1597. [CrossRef]
45. Moghadam, H.S.; Ghorbani, G.; Khedr, M.Z.; Fazlnia, N.; Chiaradia, M.; Eyuboglu, Y.; Santosh, M.; Francisco, C.G.; Martinez, M.L.; Gourgaud, A.; et al. Late Miocene K-Rich Volcanism in the Eslamieh Peninsula (Saray), NW Iran: Implications for Geodynamic Evolution of the Turkish–Iranian High Plateau. *Gondwana Res.* **2014**, *26*, 1028–1050. [CrossRef]
46. Moghadam, H.S.; Li, Q.L.; Li, X.H.; Stern, R.J.; Levresse, G.; Santos, J.F.; Lopez Martinez, M.; Ducea, M.N.; Ghorbani, G.; Hassannezhad, A. Neotethyan Subduction Ignited the Iran Arc and Back-Arc Differently. *J. Geophys. Res. Solid. Earth* **2020**, *125*, e2019JB018460. [CrossRef]
47. Shafaii Moghadam, H.; Li, Q.L.; Griffin, W.L.; Stern, R.J.; Chiaradia, M.; Karsli, O.; Ghorbani, G.; O'Reilly, S.Y.; Pourmohsen, M. Zircon U-Pb, Geochemical and Isotopic Constraints on the Age and Origin of A- and I-Type Granites and Gabbro-Diorites from NW Iran. *Lithos* **2020**, *374–375*, 105688. [CrossRef]
48. Stern, R.J.; Moghadam, H.S.; Pirouz, M.; Mooey, W. The Geodynamic Evolution of Iran. *Annu. Rev. Earth Planet. Sci.* **2021**, *49*, 9–36. [CrossRef]
49. Moghadam, H.S.; Griffin, W.L.; Santos, J.F.; Chen, R.X.; Karsli, O.; Lucci, F.; Sepidbar, F.; O'Reilly, S.Y. Geochronology, Geochemistry and Petrology of the Oligocene Magmatism in the SE Segment of the UDMB. *Iran. Lithos* **2022**, *416–417*, 106644. [CrossRef]
50. Kheirkhah, M.; Neill, I.; Allen, M.B.; Emami, M.H.; Shahraki Ghadimi, A. Distinct Sources for High-K and Adakitic Magmatism in SE Iran. *J. Asian Earth Sci.* **2020**, *196*, 104355. [CrossRef]
51. Topuz, G.; Altherr, R.; Siebel, W.; Schwarz, W.H.; Zack, T.; Hasozbek, A.; Barth, M.; Satır, M.; Cen, C. Carboniferous high-potassium I-type granitoid magmatism in the Eastern Pontides: The Gümüshane pluton (NE Turkey). *Lithos* **2010**, *116*, 92–110. [CrossRef]
52. Aghazadeh, M.; Castro, A.; Omran, N.; Emami, M.; Moinvaziri, H.; Badrzadeh, Z. The gabbro (shoshonitic)–monzonite–granodiorite association of Khankandi pluton, Alborz Mountains, NW Iran. *J. Asian Earth Sci.* **2010**, *38*, 199–219. [CrossRef]
53. Pang, K.N.; Chung, S.L.; Zarrinkoub, M.H.; Lin, Y.C.; Lee, H.Y.; Lo, C.H.; Khatib, M.M. Iranian Ultrapotassic Volcanism at 11 Ma Signifies the Initiation of Post-Collisional Magmatism in the Arabia–Eurasia Collision Zone. *Terra Nova* **2013**, *25*, 405–413. [CrossRef]
54. Lin, Y.C.; Chung, S.L.; Feyzi Bingöl, A.; Yang, L.; Okrostsvaridze, A.; Pang, K.N.; Lee, H.Y.; Lin, T.H. Diachronous Initiation of Post-Collisional Magmatism in the Arabia-Eurasia Collision Zone. *Lithos* **2020**, *356–357*, 105394. [CrossRef]
55. Azizi, H.; Daneshvar, N.; Mohammadi, A.; Asahara, Y.; Whattam, S.A.; Tsuboi, M.; Minami, M. Early Miocene Post-Collision Andesite in the Takab Area. *NW Iran. J. Pet.* **2021**, *62*, 022. [CrossRef]
56. Moghadam, H.S.; Hoernle, K.A.; Hauff, F.; Chiaradia, M.; Garbe-Schönberg, D.; Orozco-Esquivel, T.; Bindeman, I.N.; Karsli, O.; Ghorbani, G.; Mousavi, N.; et al. Middle-Late Miocene to Pleistocene Post-Collisional Magmatism in the Arabia-Eurasia Collision Zone, an Example from Northwest Iran. *J. Pet.* **2023**, *64*, 081. [CrossRef]
57. Kazemi, K.; Kananian, A.; Xiao, Y.; Sarjoughian, F. Petrogenesis of Middle-Eocene Granitoids and Their Mafic Microgranular Enclaves in Central Urmia-Dokhtar Magmatic Arc (Iran): Evidence for Interaction between Felsic and Mafic Magmas. *Geosci. Front.* **2019**, *10*, 705–723. [CrossRef]
58. Moghadam, H.S.; Rossetti, F.; Lucci, F.; Chiaradia, M.; Gerdes, A.; Martinez, M.L.; Ghorbani, G.; Nasrabady, M. The Calc-Alkaline and Adakitic Volcanism of the Sabzevar Structural Zone (NE Iran): Implications for the Eocene Magmatic Flare-up in Central Iran. *Lithos* **2016**, *248*, 517–535. [CrossRef]

59. Rossetti, F.; Nasrabady, M.; Theye, T.; Gerdes, A.; Monie, P.; Lucci, F.; Vignaroli, G. Adakite Differentiation and Emplacement in a Subduction Channel: The Late Paleocene Sabzevar Magmatism (NE Iran). *Geol. Soc. Am. Bull.* **2014**, *126*, 317–343. [CrossRef]
60. Lucci, F.; Rossetti, F.; White, J.C.; Moghadam, H.S.; Shirzadi, A.; Nasrabady, M. Tschermak fractionation in calc-alkaline magmas: The Eocene Sabzevar volcanism (NE Iran). *Arab. J. Geosci.* **2016**, *9*, 573. [CrossRef]
61. Raeisi, D.; Babazadeh, S.; Long, L.E.; Zhao, M.; Cottle, J.M.; Nayebi, N.; Modabberi, S. Geochemical and Isotopic Signatures, and Zircon U–Pb Ages of the Oldest Known Intrusive Rocks Associated with Porphyry Cu Deposits in the Central Urumieh–Dokhtar Magmatic Arc, Iran. *J. Geochem. Explor.* **2024**, *256*, 107366. [CrossRef]
62. Caillat, C.; Dehlavi, P.; Martel Jantin, B. Géologie de la Région de Saveh (Iran): Contribution à L'étude du Volcanisme et du Plutonisme Tertiaires de la Zone de l'Iran Central. Ph.D. Thesis, Université Scientifique et Médicale de Grenoble, Saint-Martin-d'Hères, France, 1978.
63. Hassanzadeh, J.; Stockli, D.F.; Horton, B.K.; Axen, G.J.; Stockli, L.D.; Grove, M.; Schmitt, A.K.; Walker, J.D. U-Pb Zircon Geochronology of Late Neoproterozoic–Early Cambrian Granitoids in Iran: Implications for Paleogeography, Magmatism, and Exhumation History of Iranian Basement. *Tectonophysics* **2008**, *451*, 71–96.
64. Ghasemi, A.; Talbot, C.J. A new tectonic scenario for the Sanandaj-Sirjan Zone (Iran). *J. Asian Earth Sci.* **2007**, *26*, 683–693. [CrossRef]
65. Goudarzi, M.; Zamanian, H.; Klotzli, U. Geochemistry and Tectono-Magmatic Setting of Hypabyssal Intrusive Rocks in the South of Mamouniyeh, Urumieh-Dokhtar Magmatic Arc, Iran. *Sci. Q. J. Geosci.* **2025**, *35*, 129–148. [CrossRef]
66. Richards, J.P.; Sholeh, A. The Tethyan Tectonic History and Cu-Au Metallogeny of Iran. *Soc. Econ. Geol. Spec. Publ.* **2016**, *19*, 193–212.
67. Kretz, R. Symbols for rock-forming minerals. *Am. Mineral.* **1983**, *68*, 277–279.
68. Middlemost, E.A.K. Naming Materials in the Magma/Igneous Rock System. *Earth Sci. Rev.* **1994**, *37*, 215–224. [CrossRef]
69. White, A.J.R.; Chappell, L.W. Granitoid Types and Their Distribution in the Lachlan Fold Belt, Southeast Australia. *Geol. Soc. Am. Mem.* **1983**, *159*, 21–34. [CrossRef]
70. Frost, B.; Barnes, C.G.; Collins, W.J.; Arculus, R.J.; Ellis, D.J.; Frost, C.D. A Geochemical Classification for Granitic Rocks. *J. Petrol.* **2001**, *42*, 2033–2048. [CrossRef]
71. Pearce, J.A.; Harris, N.B.W.; Tindle, A.G. Trace Element Discrimination Diagrams for the Tectonic Interpretation of Granitic Rocks. *J. Petrol.* **1984**, *25*, 956–983. [CrossRef]
72. Zamanian, H.; Dolatshahi, S.; Yang, X.; Karimzadeh, S.A.; Meshkani, S.A. Geochemical, Fluid Inclusion and O-H-S Isotope Constraints on the Origin of the Rangraz Copper Deposit. *Cent. Iran. Ore Geol. Rev.* **2021**, *128*, 103877. [CrossRef]
73. Goudarzi, M.; Zamanian, H.; Klötzli, U.; Ullah, M. Evidence of Boiling in Ore Forming Process Based on Quartz Textures and Fluid Inclusions Studies, a Case Study in Mamouniyeh Cu Deposit, Iran. In Proceedings of the EGU General Assembly 2024, Vienna, Austria, 14–19 April 2024. [CrossRef]
74. Goudarzi, M.; Zamanian, H.; Klötzli, U.; Lentz, D.; Ullah, M. Constraining Ore-Forming Processes Using Magnetite-Titanomagnetite Chemistry: A Case Study of the Mamuniyeh Cu Mineralization System, Urumieh-Dokhtar Magmatic Arc. *J. Econ. Geol.* **2025**. [CrossRef]
75. Goudarzi, M.; Zamanian, H.; Klötzli, U.; Ullah, M. Chemical Composition of Hydrothermal Pyrite as an Indicator for Deciphering Ore-Forming Processes: A Case Study from the Mamuniyeh Copper Deposit, UDMA. *J. Econ. Geol.* **2025**. [CrossRef]
76. Goudarzi, M.; Zamanian, H.; Klötzli, U.; Lentz, D.; Ullah, M. Genesis of the Mamuniyeh Copper Deposit in the Central Urumieh-Dokhtar Magmatic Arc, Iran: Constraints from Geology, Geochemistry, Fluid Inclusions, and H–O–S Isotopes. *Ore Geol. Rev.* **2024**, *175*, 106279. [CrossRef]
77. Goudarzi, M.; Zamanian, H.; Klötzli, U. Copper Mineralization Pattern Based on Mineralogy, Alteration, Geochemistry of Intrusive Rocks and Fluid Inclusion in the South of Mamuoniyeh, Middle Part of Urumieh-Dokhtar Magmatic Arc, Iran. *Sci. Q. J. Geosci.* **2024**, *34*, 35–62. [CrossRef]
78. Defant, M.J.; Drummond, M.S. Derivation of Some Modern Arc Magmas by Melting of Young Subducted Lithosphere. *Nature* **1990**, *347*, 662–665. [CrossRef]
79. Hammarstron, J.M.; Zen, E.A. Aluminium in Hornblende: An Empirical Igneous Geobarometer. *Am. Mineral.* **1986**, *71*, 1297–1313.
80. Rickwood, P.C. Boundary Lines within Petrologic Diagrams Which Use Oxides of Major and Minor Elements. *Lithos* **1989**, *22*, 247–263. [CrossRef]
81. Ross, P.S.; Bédard, J.H. Magmatic Affinity of Modern and Ancient Subalkaline Volcanic Rocks Determined from Trace-Element Discriminant Diagrams. *Can. J. Earth Sci.* **2009**, *46*, 823–839. [CrossRef]
82. Sun, S.; McDonough, W.F. Chemical and Isotopic Systematics of Oceanic Basalts: Implications for Mantle Composition and Processes. *Geol. Soc. Lond. Spec. Publ.* **1989**, *42*, 313–345. [CrossRef]
83. Wilson, M. *Igneous Petrogenesis Igneous Petrogenesis: A Global Tectonic Approach*; Unwin Hyman: London, UK, 1989. [CrossRef]

84. Christiansen, E.H.; Keith, J.D. Trace Element Systematics in Silicic Magmas: A Metallogenic Perspective. In *Trace Element Geochemistry of Volcanic Rocks: Applications for Massive Sulphide Exploration*; Wyman, D.A., Ed.; Short Course Notes; Geological Association of Canada: St. John's, NL, Canada, 1996; pp. 115–151.
85. Boynton, W.V. Cosmochemistry of the Rare Earth Elements, Meteorite Studies. In *Rare Earth Element Geochemistry. Developments in Geochemistry*; Henderson, P., Ed.; Elsevier: Amsterdam, The Netherlands, 1984; p. 11.
86. Deer, W.A.; Howie, R.A.; Zussman, J. *An Introduction to the Rock Forming Minerals*; Longman Scientific and Technical: London, UK, 1992.
87. Morimoto, N.; Fabries, J.; Ferguson, A.K.; Ginzburg, I.V.; Ross, M.; Seifert, F.A.; Zussman, J.; Aoki, K.; Gottardi, G. The Nomenclature of Pyroxenes. *Mineral. Mag.* **1988**, *52*, 535–550.
88. Mojzsis, S.J.; Harrison, T.M. Establishment of a 3.83-Ga Magmatic Age for the Akilia Tonalite (Southern West Greenland). *Earth Planet. Sci. Lett.* **2002**, *202*, 563–576. [CrossRef]
89. Rowley, D.B.; Xue, F.; Tucker, R.D.; Peng, Z.X.; Baker, J.; Davis, A. Ages of Ultrahigh Pressure Metamorphism and Protolith Orthogneisses from the Eastern Dabie Shan: U/Pb Zircon Geochronology. *Earth Planet. Sci. Lett.* **1997**, *151*, 191–203. [CrossRef]
90. Kirkland, C.L.; Smithies, R.H.; Taylor, R.J.M.; Evans, N.; McDonald, B. Zircon Th/U Ratios in Magmatic Environs. *Lithos* **2015**, *212–215*, 397–414. [CrossRef]
91. Wu, Y.B.; Zheng, Y.F. Study on the Genesis of Zircon and Its Restrictions on Explaining the U-Pb Age. *Chin. Sci. Bull.* **2004**, *49*, 1589–1604. [CrossRef]
92. Rubatto, D. Zircon Trace Element Geochemistry; Partitioning with Garnet and the Link between U-Pb Ages and Metamorphism. *Chem. Geol.* **2002**, *184*, 123–138. [CrossRef]
93. Pettke, T.; Audetat, A.; Schaltegger, U.; Heinrich, C.A. Magmatic-to-Hydrothermal Crystallization in the W-Sn Mineralized Mole Granite (NSW, Australia)—Part II: Evolving Zircon and Thorite Trace Element Chemistry. *Chem. Geol.* **2005**, *220*, 191–213. [CrossRef]
94. Bacon, C.R.; Sisson, T.W.; Mazdab, F.K. Young Cumulate Complex beneath Veniaminof Caldera, Aleutian Arc, Dated by Zircon in Erupted Plutonic Blocks. *Geology* **2007**, *35*, 491–494. [CrossRef]
95. Hoskin, P.W.O.; Schaltegger, U. The Composition of Zircon and Igneous and Metamorphic Petrogenesis. *Zircon. Rev. Mineral. Geochem.* **2003**, *53*, 27–62. [CrossRef]
96. Faure, G.; Mensing, T.M. The U-Pb, Th-Pb, and Pb-Pb Methods. In *Isotope Principles and Applications*; John Wiley & Sons, Inc.: Hoboken, NJ, USA, 2005; pp. 214–255.
97. Moghadam, H.S.; Griffin, W.L.; Li, X.H.; Santos, J.F.; Karsli, O.; Stern, R.J.; Ghorbani, G.; Gain, S.; Murphy, R.; O'Reilly, S.Y. Crustal Evolution of NW Iran: Cadomian Arcs, Archean Fragments and the Cenozoic Magmatic Flare-Up. *J. Pet.* **2018**, *58*, 2143–2190. [CrossRef]
98. Shaw, S.E.; Flood, R.H. Zircon Hf Isotopic Evidence for Mixing of Crustal and Silicic Mantle-Derived Magmas in a Zoned Granite Pluton, Eastern Australia. *J. Petrol.* **2009**, *50*, 147–168. [CrossRef]
99. Chiu, H.Y.; Chung, S.L.; Zarrinkoub, M.H.; Melkonyan, R.; Pang, K.N.; Lee, H.Y.; Wang, K.L.; Mohammadi, S.S.; Khatib, M.M. Zircon Hf Isotopic Constraints on Magmatic and Tectonic Evolution in Iran: Implications for Crustal Growth in the Tethyan Orogenic Belt. *J. Asian Earth Sci.* **2017**, *145*, 652–669. [CrossRef]
100. Shafaii Moghadam, H.; Corfu, F.; Chiaradia, M.; Stern, R.J.; Ghorbani, G. Sabzevar Ophiolite, NE Iran: Progress from Embryonic Oceanic Lithosphere into Magmatic Arc Constrained by New Isotopic and Geochemical Data. *Lithos* **2014**, *210–211*, 224–241. [CrossRef]
101. Müller, D.; Groves, D.I. *Potassic Igneous Rocks and Associated Gold–Copper Mineralization*, 3rd ed.; Springer: Berlin, Germany, 1997.
102. Sarjoughian, F.; Kananian, A.; Ahmadian, J.; Murata, M. Chemical Composition of Biotite from the Kuh-e Dom Pluton, Central Iran: Implication for Granitoid Magmatism and Related Cu-Au Mineralization. *Arab. J. Geosci.* **2015**, *8*, 1521–1533. [CrossRef]
103. Zarasvandi, A.; Rezaei, M.; Sadeghi, M.; Lentz, D.; Adelpour, M.; Pourkaseb, H. Rare Earth Element Signatures of Economic and Sub-Economic Porphyry Copper Systems in Urumieh-Dokhtar Magmatic Arc (UDMA. *Iran. Ore Geol. Rev.* **2015**, *70*, 407–423. [CrossRef]
104. Fazeli, B.; Khalili, M.; Köksal, F.T.; Mansouri Esfahani, M.; Beavers, R. Petrological Constraints on the Origin of the Plutonic Massif of the Ghaleh Yaghmesh Area, Urumieh-Dokhtar Magmatic Arc, Iran. *J. Afr. Earth Sci.* **2017**, *129*, 233–247. [CrossRef]
105. Eby, G.N. Chemical Subdivision of the A-Type Granitoids: Petrogenetic and Tectonic Implications. *Geology* **1992**, *20*, 641–644. [CrossRef]
106. Green, N.L. Influence of Slab Thermal Structure on Basalt Source Regions and Melting Conditions: REE and HFSE Constraints from Garibaldi Volcanic Belt, Northern Cascadia Subduction System. *Lithos* **2006**, *87*, 23–49. [CrossRef]
107. Thieblemont, D.; Tegyey, M. Une discrimination géochimique des roches différenciées témoin de la diversité origine et de situation tectonique des magmas calco-alcalins. *Comptes Rendus l'Académie Sci.* **1994**, *319*, 87–94.
108. Morata, D.; Oliva, C.; Cruz, R.; Suarez, M. The Bandurrias gabbro; late Oligocene alkaline magmatism in the Patagonian Cordillera. *J. Am. Earth Sci.* **2005**, *18*, 147–162.

109. Sisson, T.W.; Grove, T.L. Temperatures and H_2O Contents of Low-MgO High-Alumina Basalts. *Contrib. Mineral. Petrol.* **1993**, *113*, 167–184. [CrossRef]
110. Moghadam, H.S.; Li, X.-H.; Ling, X.-X.; Santos, J.F.; Stern, R.J.; Li, Q.-L.; Ghorbani, G. Eocene Kashmar Granitoids (NE Iran): Petrogenetic Constraints from U–Pb Zircon Geochronology and Isotope Geochemistry. *Lithos* **2015**, *216–217*, 118–135. [CrossRef]
111. Pearce, J.A. Geochemical Fingerprinting of Oceanic Basalts with Applications to Ophiolite Classification and the Search for Archean Oceanic Crust. *Lithos* **2008**, *100*, 14–48. [CrossRef]
112. Schandl, E.S.; Gorton, M.P. Application of High Field Strength Elements to Discriminate Tectonic Settings in VMS Environments. *Econ. Geol.* **2002**, *97*, 629–642. [CrossRef]
113. Castillo, P.R. Origin of the Adakite-High-Nb Basalt Association and Its Implications for Post-Subduction Magmatism in Baja California, Mexico. *Geol. Soc. Am. Bull.* **2008**, *120*, 451–462. [CrossRef]
114. Brandl, P.A.; Hamada, M.; Arculus, R.J.; Johnson, K.; Marsaglia, K.M.; Savov, I.P.; Ishizuka, O.; Li, H. The Arc Arises: The Links between Volcanic Output, Arc Evolution, and Melt Composition. *Earth Planet. Sci. Lett.* **2017**, *461*, 73–84. [CrossRef]
115. Tatsumi, Y. Slab Melting: Its Role in Continental Crust Formation and Mantle Evolution. *Geophys. Res. Lett.* **2000**, *27*, 3941–3944. [CrossRef]
116. Kirchenbaur, M.; Münker, C.; Schuth, S.; Garbe-Schonberg, D.; Marchev, P. Tectonomagmatic Constraints on the Sources of Eastern Mediterranean K-Rich Lavas. *J. Petrol.* **2012**, *53*, 27–65. [CrossRef]
117. Woodhead, J.; Eggins, S.; Johnson, R. Magma Genesis in the New Britain Island Arc: Further Insights into Melting and Mass Transfer Processes. *J. Petrol.* **1998**, *39*, 1641–1668. [CrossRef]
118. Pearce, J.A.; Peate, D.W. Tectonic Implications of the Composition of Volcanic ARC Magmas. *Annu. Rev. Earth Planet. Sci.* **1995**, *23*, 251–285. [CrossRef]
119. Furman, T.; Graham, D. Erosion of Lithospheric Mantle beneath the East African Rift System: Geochemical Evidence from the Kivu Volcanic Province. *Lithos* **1999**, *48*, 237–262. [CrossRef]
120. Ionov, D.A.; Hofmann, A.W. Nb-Ta-Rich Mantle Amphiboles and Micas: Implications for Subduction-Related Metasomatic Trace Element Fractionations. *Earth Planet. Sci. Lett.* **1999**, *131*, 341–356. [CrossRef]
121. Aldanmaz, E.; Pearce, J.A.; Thirlwall, M.F.; Mitchell, J.G. Petrogenetic Evolution of Late Cenozoic, Post-Collision Volcanism in Western Anatolia, Turkey. *J. Volcanol. Geotherm. Res.* **2000**, *102*, 67–95. [CrossRef]
122. Li, J.X.; Qin, K.; Li, G.M.; Xiao, B.; Chen, L.; Zhao, J.X. Post-Collisional Ore Bearing Adakitic Porphyries from Gangdese Porphyry Copper Belt, Southern Tibet: Melting of Thickened Juvenile Arc Lower Crust. *Lithos* **2011**, *126*, 265–277. [CrossRef]
123. McKenzie, D.; O'Nions, R.K. Partial Melt Distributions from Inversion of Rare Earth Element Concentration. *J. Petrol.* **1991**, *32*, 1021–1091. [CrossRef]
124. Ferlito, C. Bimodal Geochemical Evolution at Sheveluch Stratovolcano, Kamchatka, Russia: Consequence of a Complex Subduction at the Junction of the Kuril Kamchatka and Aleutian Island Arcs. *Earth Sci. Rev.* **2011**, *105*, 49–69. [CrossRef]
125. Shaw, D.M. Trace Element Fractionation during Anatexis. *Geochim. Cosmochim. Acta* **1970**, *34*, 237–243. [CrossRef]
126. Hawkesworth, C.J.; Gallager, K.; Hergt, J.M.; McDermott, F. Destructive plate margin magmatism: Geochemistry and melt generation. *Lithos* **1994**, *33*, 169–188. [CrossRef]
127. D'Orazio, M.; Agostini, S.; Innocenti, F.; Haller, M.J.; Manetti, P.; Mazzarini, F. Slab Window Related Magmatism from Southernmost South America: The Late Miocene Mafic Volcanics from the Estancia Glencross Area (52°S, Argentina–Chile). *Lithos* **2001**, *57*, 67–89. [CrossRef]
128. Beccaluva, L.; Macciotta, G.; Piccardo, G.; Zeda, O. Clinopyroxene Composition of Ophiolite Basalts as Petrogenetic Indicator. *Chem. Geol.* **1989**, *77*, 165–182. [CrossRef]
129. Nisbet, E.G.; Pearce, J.A. Clinopyroxene Composition of Mafic Lavas from Different Tectonic Settings. *Contrib. Mineral. Petrol.* **1977**, *63*, 161–173. [CrossRef]
130. Schweitzer, E.L.; Papike, J.J.; Bence, A.E. Statistical Analysis of Clinopyroxenes from Deep-Sea Basalts. *Am. Mineral.* **1979**, *64*, 501–513. [CrossRef]
131. Parlak, O.; Bağci, U.; Rizaoğlu, T.; Ionescu, C.; Onal, G.; Hock, V.; Kozlu, H. Petrology of Ultramafic to Mafic Cumulate Rocks from the Goksun (Kahramanmaraş) Ophiolite, Southeast Turkey. *Geosci. Front.* **2020**, *11*, 109–128. [CrossRef]
132. DeBari, S.M.; Coleman, R.G. Examination of the Deep Levels of an Island Arc: Evidence from the Tonsina Ultramafic-Mafic Assemblage, Tonsina, Alaska. *J. Geophys. Res. Solid. Earth* **1989**, *94*, 4373–4391. [CrossRef]
133. Elthon, D. Petrology of Gabbroic Rocks from the Mid-Cayman Rise Spreading Center. *J. Geophys. Res. Solid. Earth* **1987**, *92*, 658–682. [CrossRef]
134. Soesoo, A. A Multivariate Statistical Analysis of Clinopyroxene Composition: Empirical Coordinates for the Crystallization PT-Estimations. *Geol. Soc. Swed. Geol. Fören.* **1997**, *119*, 55–60. [CrossRef]
135. Arculus, R.J. Supra-Subduction Zone Pyroxenites from San Jorge and Santa Isabel (Solomon Islands). *J. Petrol.* **2006**, *47*, 1531–1555. [CrossRef]

136. Aparicio, A. Relationship between Clinopyroxene Composition and the Formation Environment of Volcanic Host Rocks. *IUP J. Earth Sci.* **2010**, *4*, 34–44.
137. Castillo, P.R.; Janney, P.E.; Solidum, R.U. Petrology and Geochemistry of Camiguin Island, Southern Philippines: Insights to the Source of Adakites and Other Lavas in a Complex Arc Setting. *Contrib. Miner. Pet.* **1999**, *134*, 33–51. [CrossRef]
138. Wang, X.C.; Wilde, S.A.; Li, Q.L.; Yang, Y.N. Continental Flood Basalts Derived from the Hydrous Mantle Transition Zone. *Nat. Commun.* **2015**, *6*, 7700. [CrossRef]
139. Rollinson, H.R. *Using Geochemical Data: Evaluation, Presentation, Interpretation*; Longman Scientific and Technical: New York, NY, USA, 1993.
140. Rudnick, R.L.; Gao, S. Composition of the Continental Crust. In *Treatise on Geochemistry*; Rudnick, R.L., Ed.; Elsevier: Amsterdam, The Netherlands, 2003; Volume 3, pp. 1–64.
141. Michelfelder, G.S.; Feeley, T.C.; Wilder, A.D.; Klemetti, E.W. Modification of the Continental Crust by Subduction Zone Magmatism and Vice-Versa: Across-Strike Geochemical Variations of Silicic Lavas from Individual Eruptive Centers in the Andean Central Volcanic Zone. *Geosciences* **2013**, *3*, 633–667. [CrossRef]
142. Guo, K.; Zhai, S.; Yu, Z.; Zeng, Z.; Wang, X.; Yin, X. Geochemical Characteristics of Major and Trace Elements in the Okinawa Trough Basaltic Glass. *Acta Oceanol. Sin.* **2018**, *37*, 14–24. [CrossRef]
143. Srivastava, R.K.; Singh, S.K.; Samal, A.K. Geochemistry and Geodynamic Implications of the Mafic Magmatic Plumbing System of the ca. 1.98–1.97 Ga Jhansi Large Igneous Province in the Northern Indian Shield. *J. Earth Syst. Sci.* **2022**, *131*, 4. [CrossRef]
144. Temel, A.; Gundogdu, A.; Gourgaud, M.N. Petrological and Geochemical Characteristics of Cenozoic High-K Calc-Alkaline Volcanism in Konya, Central Anatolia, Turkey. *J. Volcanol. Geotherm. Res.* **1998**, *85*, 327–354. [CrossRef]
145. Alici, P.; Temel, A.; Gourgaud, A.; Vidal, P.; Gündoğdu, M.N. Quaternary Tholeiitic to Alkaline Volcanism in the Karasu Valley, Dead Sea Rift Zone, Southeast Turkey: Sr-Nd-Pb-O Isotopic and Trace-Element Approaches to Crust-Mantle Interaction. *Int. Geol. Rev.* **2001**, *43*, 120–138. [CrossRef]
146. Ahmadzadeh, G.; Jahangiri, A.; Lentz, D.; Mojtahedi, M. Petrogenesis of Plio-Quaternary Post-Collisional Ultrapotassic Volcanism in NW of Marand, NW Iran. *J. Asian Earth Sci.* **2010**, *39*, 37–50. [CrossRef]
147. Castro, A.; Aghazadeh, M.; Badrzadeh, Z.; Chichorro, M. Late Eocene–Oligocene Post-Collisional Monzonitic Intrusions from the Alborz Magmatic Belt, NW Iran. An Example of Monzonite Magma Generation from a Metasomatized Mantle Source. *Lithos* **2013**, *180–181*, 109–127. [CrossRef]
148. Blundy, J.; Wood, B. Partitioning of Trace Elements between Crystals and Melts. *Earth Planet. Sci. Lett.* **2003**, *210*, 383–397. [CrossRef]
149. Davidson, J.; Turner, S.; Handley, H.; Macpherson, C.; Dosseto, A. Amphibole "sponge" in arc crust? *Geology* **2007**, *35*, 787–790. [CrossRef]
150. Peccerillo, A.; Barberio, M.R.; Yirgu, G.; Ayalew, D.; Barbieri, M.; Wu, T.W. Relationships between Mafic and Peralkaline Silicic Magmatism in Continental Rift Settings: A Petrological, Geochemical, and Isotopic Study of the Gedemsa Volcano. *Cent. Ethiop. Rift. J. Petrol.* **2003**, *44*, 2003–2032. [CrossRef]
151. Patchett, P.J.; Kouvo, O.; Hedge, C.E.; Tatsumoto, M. Evolution of Continental Crust and Mantle Heterogeneity: Evidence from Hf Isotopes. *Contrib. Mineral. Petrol.* **1981**, *77*, 279–297. [CrossRef]
152. Corfu, F.; Stott, G.M. Age and Petrogenesis of Two Late Archean Magmatic Suites, Northwestern Superior Province, Canada: Zircon U-Pb and Lu-Hf Isotopic Relations. *J. Petrol.* **1993**, *34*, 817–883.
153. Kemp, A.I.S.; Hawkesworth, C.J.; Foster, G.L.; Paterson, B.A.; Woodhead, J.D.; Hergt, J.M.; Gray, C.M.; Whitehouse, M.J. Magmatic and Crustal Differentiation History of Granitic Rocks from Hf–O Isotopes in Zircon. *Science* **2007**, *315*, 980–983. [CrossRef] [PubMed]
154. Nutman, A.P.; Mohajjel, M.; Bennett, V.C.; Fergusson, C.L. Gondwanan Eoarchean-Neoproterozoic Ancient Crustal Material in Iran and Turkey: Zircon U–Pb–Hf Isotopic Evidence. *Can. J. Earth Sci.* **2014**, *51*, 272–285. [CrossRef]
155. Ustaömer, P.A.; Ustaömer, T.; Collins, A.S.; Robertson, A.H.F. Cadomian (Ediacaran–Cambrian) Arc Magmatism in the Bitlis Massif, SE Turkey: Magmatism along the Developing Northern Margin of Gondwana. *Tectonophysics* **2009**, *473*, 99–112. [CrossRef]
156. Yilmaz Şahin, S.; Aysal, N.; Güngör, Y.; Peytcheva, I.; Neubauer, F. Geochemistry and U–Pb zircon geochronology of metagranites in Istranca (Strandja) Zone, NW Pontides, Turkey: Implications for the geodynamic evolution of Cadomian orogeny. *Gondwana Res.* **2014**, *26*, 755–777. [CrossRef]
157. Stern, R.J.; Ali, K.A.; Ren, M.; Jarrar, G.H.; Romer, R.L.; Leybourne, M.I.; Whitehouse, M.J.; Ibrahim, K.M. Cadomian (560Ma) Crust Buried beneath the Northern Arabian Peninsula: Mineral, Chemical, Geochronological, and Isotopic Constraints from NE Jordan Xenoliths. *Earth Planet. Sci. Lett.* **2016**, *436*, 31–42. [CrossRef]
158. Rezaei, L.; Timmerman, M.J.; Altenberger, U.; Moazzen, M.; Wilke, F.D.H.; Günter, C.; Sudo, M.; Sláma, J. Ediacaran to Jurassic Geodynamic Evolution of the Alborz Mountains, North Iran: Geochronological Data from the Gasht Metamorphic Complex. *Swiss J. Geosci.* **2024**, *117*, 13. [CrossRef]

159. Ramezani, J.; Tucker, R.D. The Saghand Region, Central Iran: U-Pb Geochronology, Petrogenesis and Implications for Gondwana Tectonics. *Am. J. Sci.* **2003**, *303*, 622–665. [CrossRef]
160. Azizi, H.; Whattam, S.A. Does Neoproterozoic-Early Paleozoic (570–530 Ma) Basement of Iran Belong to the Cadomian Orogeny? *Precambrian Res.* **2022**, *368*, 106474. [CrossRef]
161. Sepidbar, F.; Homam, S.M.; Wu, G.; Moritz, R.; Hafezimoghadas, H. Early Paleozoic Mafic Intraplate Magmatism in the Binaloud Zone, NE Iran: Implications for the Long-Lived Mantle Plume Activity in the Northern Margin of Gondwana. *Lithos* **2023**, *450–451*, 107191. [CrossRef]
162. Doroozi, R.; Vaccaro, C.; Masoudi, F.; Petrini, R. Petrogenesis and Mantle Source Characteristics of Triassic Alkaline Basaltic Rocks of North Kamarbon, Northern Central Alborz, Iran. *Solid. Earth Sci.* **2018**, *3*, 115–129. [CrossRef]
163. Maghdour-Mashhour, R.; Hayes, B.; Pang, K.N.; Bolhar, R.; Tabbakh Shabani, A.A.; Elahi-Janatmakan, F. Episodic subduction initiation triggered Jurassic magmatism in the Sanandaj–Sirjan zone. *Iran. Lithos* **2021**, *396–397*, 106189. [CrossRef]
164. Shirdashtzadeh, N.; Dilek, Y.; Furnes, H.; Dantas, E.L. Early Jurassic and Late Cretaceous Plagiogranites in Nain–Baft Ophiolitic Mélange Zone in Iran: Remnants of Rift–Drift and SSZ Evolution of a Neotethyan Seaway. *J. Geol. Soc.* **2024**, *181*, 2023–2181. [CrossRef]
165. Jamshidi, F.; Mortazavi, M.; Asiabanha, A.; Santos, J. Late Cretaceous volcanism in the northern Urumieh-Dokhtar Magmatic Arc, central Iran. *Neues Jahrb. Mineral. Abh.* **2024**, *199*, 1–17. [CrossRef]
166. Hosseini, M.R.; Hassanzadeh, J.; Alirezaei, S.; Sun, W.; Li, C.Y. Age Revision of the Neotethyan Arc Migration into the Southeast Urumieh-Dokhtar Belt of Iran: Geochemistry and U–Pb Zircon Geochronology. *Lithos* **2017**, *284–585*, 296–309. [CrossRef]
167. Moradi, S.; Christiansen, E.H.; Jiang, S.Y.; Ghorbani, M.R. Petrogenesis and Tectonic Implications of Cenozoic Mafic Volcanic Rocks in the Kahak Area of Central Urumieh–Dokhtar Magmatic Arc, Iran. *J. Asian Earth Sci.* **2022**, *239*, 105404. [CrossRef]
168. Raeisi, D.; Mirnejad, H.; McFarlane, C.; Sheibi, M.; Babazadeh, S. Geochemistry and Zircon U-Pb Geochronology of Miocene Plutons in the Urumieh-Dokhtar Magmatic Arc, East Tafresh. *Cent. Iran. Int. Geol. Rev.* **2019**, *62*, 1815–1827. [CrossRef]
169. Lechmann, A.; Burg, J.-P.; Ulmer, P.; Guillong, M.; Faridi, M. Metasomatized Mantle as the Source of Mid-Miocene-Quaternary Volcanism in NW-Iranian Azerbaijan: Geochronological and Geochemical Evidence. *Lithos* **2018**, *304*, 311–328. [CrossRef]
170. Ghalamghash, J.; Schmitt, A.K.; Chaharlang, R. Age and Compositional Evolution of Sahand Volcano in the Context of Post-Collisional Magmatism in Northwestern Iran: Evidence for Time Transgressive Magmatism Away from the Collisional Suture. *Lithos* **2019**, *344–345*, 265–279. [CrossRef]
171. Belousova, E.A.; Jimenez, J.M.G.; Graham, I.; Griffin, W.L.; O'Reilly, S.Y.; Pearson, N.; Martin, L.; Carven, S.; Talavera, C. The Enigma of Crustal Zircons in Upper-Mantle Rocks: Clues from the Tumut Ophiolite, Southeast Australia. *Geology* **2015**, *43*, 119–122. [CrossRef]
172. Mouthereau, F.; Lacombe, O.; Vergés, J. Building the Zagros Collisional Orogen: Timing, Strain Distribution and the Dynamics of Arabia/Eurasia Plate Convergence. *Tectonophysics* **2012**, *532–535*, 27–60. [CrossRef]
173. Babazadeh, S.; Raeisi, D.; Santosh, M.; Zhao, M.; D'Antonio, M. Recycled Mantle Source for Porphyry Mineralization: U−Pb and Re−Os Geochronology, and S–Pb–Cu Isotopic Constraints from the Urumieh-Dokhtar Magmatic Arc, Central Iran. *J. Geochem. Explor.* **2025**, *268*, 107630. [CrossRef]
174. Raeisi, D.; Zhao, M.; Babazadeh, S.; Long, L.E.; Hajsadeghi, S.; Modabberi, S. Synthesis on Productive, Sub Productive and Barren Intrusions in the Urumieh–Dokhtar Magmatic Arc, Iran, Constrains on Geochronology and Geochemistry. *Ore Geol. Rev.* **2021**, *132*, 103997. [CrossRef]
175. Agard, P.; Omrani, J.; Jolivet, L.; Whitechurch, H.; Vrielynck, B.; Spakman, W.; Monié, P.; Meyer, B.; Wortel, R. Zagros Orogeny: A Subduction-Dominated Process. *Geol. Mag.* **2011**, *148*, 692–725. [CrossRef]
176. Shahsavari Alavijeh, B.; Rashidnejad Omran, N.; Toksoy Kökçal, F.; Xu, W.; Ghalamghash, J. Oligocene Subduction-Related Plutonism in the Nodoushan Area, Urumieh-Dokhtar Magmatic Belt: Petrogenetic Constraints from U-Pb Zircon Geochronology and Isotope Geochemistry. *Geosci. Front.* **2019**, *10*, 725–751. [CrossRef]
177. Haschke, M.R.; Scheuber, E.; Gunther, A.; Reutter, K.-J. Evolutionary Cycles during the Andean Orogeny: Repeated Slab Breakoff and Flat Subduction? *Terra Nova* **2002**, *14*, 49–55. [CrossRef]
178. Dumitru, T.A.; Gans, P.B.; Foster, D.A.; Miller, E.L. Refrigeration of the Western Cordilleran Lithosphere during Laramide Shallow-Angle Subduction. *Geology* **1991**, *19*, 1145–1148. [CrossRef]

Disclaimer/Publisher's Note: The statements, opinions and data contained in all publications are solely those of the individual author(s) and contributor(s) and not of MDPI and/or the editor(s). MDPI and/or the editor(s) disclaim responsibility for any injury to people or property resulting from any ideas, methods, instructions or products referred to in the content.